

# 1 ORCAS Keck Instrument Demonstrator

2 Eliad Peretz<sup>a</sup>, Peter Wizinowich<sup>b</sup>, Maxwell A. Millar-Blanchaer<sup>c</sup>, Bert Pasquale<sup>a</sup>, Jason  
3 Chin<sup>b</sup>, Guillaume Filion<sup>d</sup>, Luke Gers<sup>b</sup>, Shui Hung Kwok<sup>b</sup>, Jean Thomas Landry<sup>d</sup>, Scott  
4 Lilley<sup>b</sup>, Eduardo Marin<sup>b</sup>, Sam Ragland<sup>b</sup>, Ed Wetherell<sup>b</sup>, Kevin Hall<sup>a</sup>, J. Fowler<sup>e</sup>, Étienne  
5 Gauvin<sup>d</sup>, Rebecca Jensen-Clem<sup>e</sup>, Marc Kassis<sup>b</sup>, Peter Kurczynski<sup>a</sup>, John Mather<sup>a</sup>, Eric L.  
6 Nielsen<sup>i</sup>, John O’Meara<sup>b</sup>, Imke de Pater<sup>g</sup>, Peter Plavchan<sup>f</sup>, Steph Sallum<sup>h</sup>, Shobita  
7 Satyapal<sup>f</sup>, Brett Smith<sup>b</sup>, Kayla Carmical<sup>a</sup>, Jack Grossman<sup>c</sup>, Andrew Lewis<sup>a</sup>, Maya  
8 Wertheim<sup>a</sup>, Vivian Palmer<sup>a</sup>

9 <sup>a</sup>NASA Goddard Space Flight Center, Greenbelt, MD 20771, USA

10 <sup>b</sup>W. M. Keck Observatory, Kamuela, HI 96743, USA

11 <sup>c</sup>University of California Santa Barbara, CA 91125, USA

12 <sup>d</sup>OMP Inc., Quebec City, QC, G1K 4L2, Canada

13 <sup>e</sup>University of California, Santa Cruz, Santa Cruz, CA 95064, USA

14 <sup>f</sup>George Mason University, Fairfax, Virginia 22030, USA

15 <sup>g</sup>University of California, Berkeley, Berkeley, CA, USA

16 <sup>h</sup>University of California Irvine, Irvine, CA 92697, USA-

17 <sup>i</sup>New Mexico State University, Las Cruces, NM 88003, USA

18 **Abstract.** The Orbiting Configurable Artificial Star (ORCAS) mission in collaboration with the W. M. Keck Obser-  
19 vatory (WMKO) have designed, assembled, built and delivered, within 180 days, ORKID (ORCAS Keck Instrument  
20 Demonstrator), an early visible-wavelength performance demonstration with the Keck II Adaptive Optics (AO) sys-  
21 tem. The optical performance of ORKID meets the technical requirements derived from science goals of having a  
22 Nyquist sampled point spread function (PSF) at 650 nm. This is achieved by diffraction-limited as-built performance  
23 with an RMS (root mean square) internal wavefront error below 50 nm, which is key for the advancement of the OR-  
24 CAS mission. ORKID has acquired, with a closed AO loop, no frame selection, while shifting and adding, the sharpest  
25 ever on-sky image captured at Keck II. With a FWHM of  $\sim 15$  mas, this is the equivalent of a 9 m diffraction-limited  
26 telescope. By doing so, the immense potential and viability of the proposed Hybrid observatory ORCAS mission is  
27 demonstrated.

28 **Keywords:** ORCAS, W. M. Keck Observatory, Adaptive Optics, Artificial Guide Star, Orbiting Guide Star, Wavefront  
29 Correction, Visible Instrument, Hybrid Observatories.

30 \*Eliad Peretz, [eliad.peretz@nasa.gov](mailto:eliad.peretz@nasa.gov)

## 31 1 Introduction

32 The ORCAS mission<sup>1-5</sup> is a first-of-its-kind hybrid space and ground observatory. It aims to com-  
33 plement and enable, at a SmallSat budget, new science accessible to future flagship-class missions  
34 over a decade from now (See figure 1). This science would be enabled by the unprecedented  
35 angular resolution and sensitivity provided by ORCAS-enabled AO-corrected observations with  
36 large ground-based telescopes.<sup>6</sup> The ORCAS mission would provide a bright point source for AO  
37 wavefront sensing, tuneable across a large range of magnitudes (0<sup>th</sup> through 8<sup>th</sup>) and wavelengths  
38 (532 nm, 778 nm, 1064 nm and 1550 nm), allowing correction at visible and near infrared (NIR)  
39 wavelengths with the WMKO AO systems.<sup>7,8</sup> The low-cost ORCAS mission operating in col-  
40 laboration with the W. M. Keck Observatory (WMKO) would provide Great Observatory quality  
41 capabilities (in the league of major space telescopes) open to all US observers via a community-  
42 driven observation plan. These observations would result in unique science for the mission, while

43 also complementing and extending the science capabilities of HST, JWST, Roman, and other po-  
44 tential future missions.

45 Observations from space with Hubble, and now JWST, leverage their angular resolution and  
46 sensitivity abilities to perform major discoveries about our Universe. These observatories rely on  
47 large ground observatories for follow-up observations. Telescopes such as the Keck Observatory  
48 rely on Adaptive Optics (AO) to partially correct the atmospheric turbulence that blurs their images.  
49 There are two primary methods to perform AO observations: (1) Natural Guide Stars (NGS) and  
50 (2) Laser Guide Stars (LGS). If a star of suitable brightness is within the vicinity of a desired  
51 science target, the observatory can lock-on to it to perform corrections. NGS typically delivers  
52 the highest Strehl ratios, but the bright light from the guide star hinders the contrast. However,  
53 99% of the sky is out of reach for NGS since there is a limited number of suitable stars. In the  
54 absence of a bright star near the chosen science target, the observer can create an artificial star by  
55 pointing a sodium (Na) laser, which excites the sodium layer. LGS observations suffer primarily  
56 from the Cone Effect, where the atmospheric turbulence effecting a star's wavefront is cylindrical,  
57 but the wavefront measured by the LGS is conical. As a result of that, among other reasons, only  
58 a partial correction can be performed.<sup>8</sup> The ORCAS mission can push the boundaries of ground-  
59 based AO observations by: (1) Providing a bright enough "artificial" NGS near any science target,  
60 (2) rejecting the bright laser from the ORCAS payload with a narrowband filter to maintain high  
61 contrast.

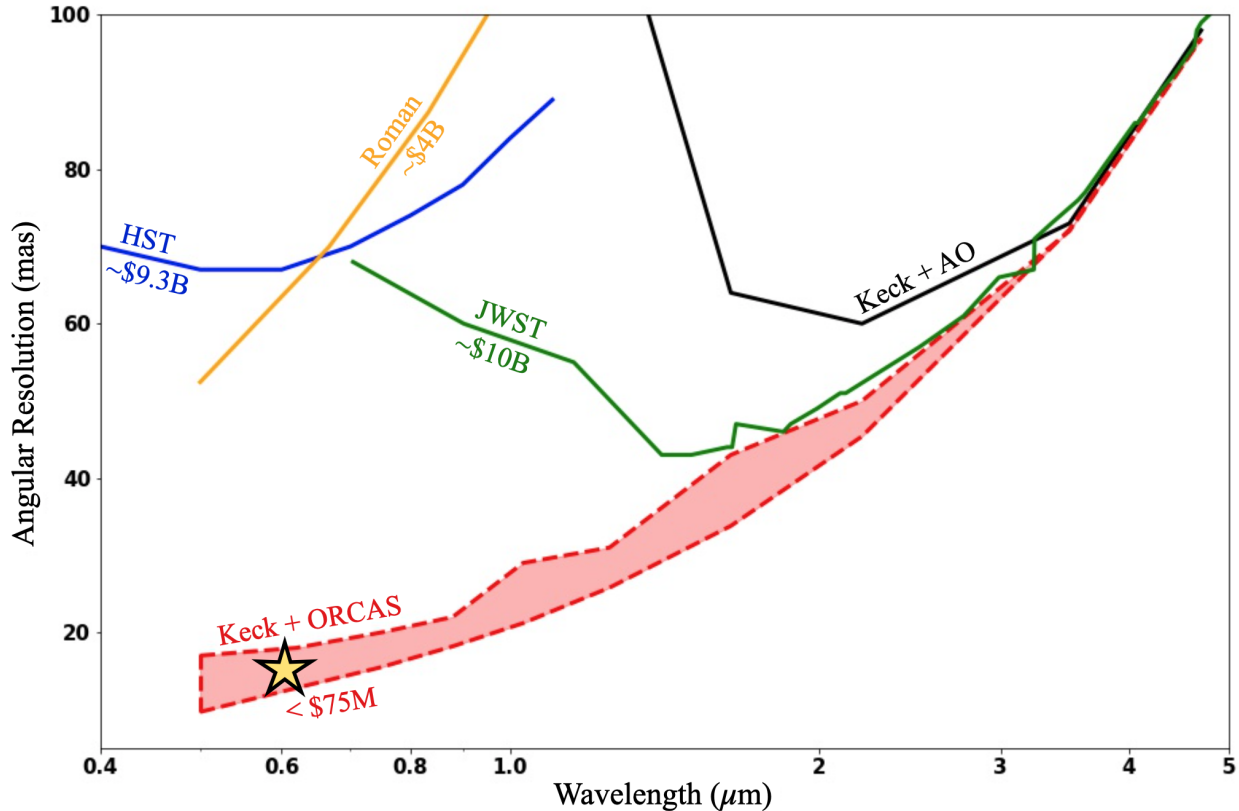


**Fig 1** Predicted Angular Resolution vs wavelength of selected future space missions/observatories. The region marked in red was predicted by the ORCAS mission as of 2020, the star indicates the ORKID system performance depicted in this paper. Predicted project budgets are provided for context. Notice that in principle a guidestar can be used by many other ground station like ELT/VLT/Subaru, for each one a different region of increased performance can be estimated. All data from previous and upcoming missions are drawn from their respective mission and/or instrument reports.

62 The ORKID project, a technology demonstrator for the ground segment, was developed to  
 63 show the visible-wavelength performance potential of a bright source with the Keck II AO system,  
 64 which is a part of a three stage technology development program effort which also includes AO  
 65 imaging science targets with asteroids as moving guide stars, and ultimately the usage of laser-  
 66 carrying spacecraft operating in conjugation with Keck AO system. This demonstration (ORKID)  
 67 has been successfully achieved with 15.2 mas FWHM images at 650 nm. Two NSF-funded up-  
 68 grades to the Keck II AO system are underway which will reduce the fitting error (replacing the  
 69 current 349-actuator deformable mirror with a 2,844-actuator deformable mirror) and bandwidth  
 70 error (replacing the real-time computer with a machine capable of 1 ms control iterations<sup>9</sup>) of the  
 71 current system, facilitating higher performance when using bright guide stars. Another ORKID  
 72 demonstration underway is the use of moving asteroids for AO correction and implementing track-  
 73 ing wavefront sensors to keep a background target fixed on the science instrument, as well as  
 74 post processing of the data. These demonstration will advance the ground system operational and  
 75 technological readiness level to the adequate level to propose the ORCAS mission. Ultimately, the  
 76 ORCAS mission will provide the Keck II AO system with the capability to access “locked regions”  
 77 of the night sky (i.e., regions of interest without access to nearby bright natural guide stars), and  
 78 near diffraction limited performance at a wide range of wavelengths.

79 In this paper we establish the scientific and programmatic goals for ORKID in section 2, for-  
80 mulate the instrument engineering requirements in section 3, provide details of the optical and  
81 mechanical design of the instrument in section 4, and conduct performance analysis in section 5.  
82 Finally, we share preliminary on-sky results in section 6, while leaving a detailed characterization  
83 of the visible-light AO performance and other instrument parameters for future work.

## 84 **2 Scientific and Programmatic Goals**

### 85 *2.1 Science*

86 Here we highlight the primary science cases for ORKID, broken up into four main groups: Solar  
87 System in section 2.1.1, Binary Stars in section 2.1.2, and Accreting Exoplanets in section 2.1.3.  
88 for additional context, the full ORCAS mission science traceability matrix (STM) please see the  
89 ORCAS AS3 report.<sup>6</sup>

#### 90 *2.1.1 Solar System Science*

91 In the decades since the Voyager spacecraft flew past Neptune and Uranus,<sup>10,11</sup> the two planets have  
92 changed significantly. Uranus, initially devoid of significant cloud features, has revealed several  
93 large cloud features since the planet's north pole came into view.<sup>12</sup> Most intriguing are the polar  
94 cloud features which have been detected in the H-band (1.63  $\mu\text{m}$ ), which can be discerned if the  
95 spatial resolution is high enough.<sup>13</sup> Neptune, on the other hand, has demonstrated a continuous  
96 evolution, with dark spots and huge storms (i.e., extremely bright clouds) infrequently appearing  
97 and disappearing.<sup>e.g.14,15</sup> Understanding the atmospheric dynamics that cause these features is a  
98 key step in understanding the detailed atmospheric structure of these planets, and progress can  
99 only be made through multi-wavelength (and hence multi-pressure-level) monitoring.

100 Ground-based observations in visible wavelengths would bring a wealth of additional infor-  
101 mation to ground-based near-infrared (NIR) observations, since different atmospheric depths are  
102 probed at different wavelengths. ORKID will enable monitoring of the two planets in and out  
103 of the methane band at wavelengths 889 and 643 nm, respectively. The contrast between clouds  
104 and background is highest at 889 nm, where we probe near the tropopause, while deeper layers  
105 are probed at 643 nm. This data can be compared with NIR images, and extend wavelength (i.e.  
106 altitude) coverage of previous Keck data.

107 Titan's atmosphere consists primarily of  $\text{N}_2$  gas with a few percent  $\text{CH}_4$ . Since Titan's surface  
108 temperature is close to the triple point of  $\text{CH}_4$ , this compound behaves like water on Earth. A  
109 dense haze layer, produced via photolysis of  $\text{CH}_4$ , prevents probing the surface, except at a few  
110 wavelengths in the infrared (IR) and at 940 nm. ORKID will observe both at 889 and 940 nm  
111 to probe both the atmosphere and surface, respectively. It is expected that these atmospheric and  
112 surface maps will produce the highest resolution features since Cassini, allowing us to search for  
113 changes in time.

114 Io is a most fascinating satellite; it is the most volcanically active body in our Solar System, and  
115 the only body with a  $\text{SO}_2$ -dominated atmosphere. Numerous volcanic eruptions have been detected  
116 at near-IR wavelengths through hot spot (hot lava) emissions (e.g., 16). Several spacecraft missions  
117 have detected plumes associated with some hot spots, either directly and/or through changes in  
118 color on the satellite's surface. ORKID could potentially characterize changes on Io's surface as  
119 well as observe plumes directly.

120 Finally, due to the higher spatial resolution with Keck in the visible than the near-IR, ORKID  
121 observations could include small bodies, such as asteroids and Kuiper Belt objects, which would  
122 allow for excellent shape determination and detection of moonlets and rings.

### 123 2.1.2 *Binary Stars*

124 With the high spatial resolution afforded by ORKID in the visible spectrum, new stellar binaries  
125 can be imaged and the orbits of known binaries have the potential to be monitored with higher  
126 astrometric precision as compared to the infrared. This could benefit a range of binary star science  
127 cases, including the dynamic measurement of stellar masses. Here we motivate one impactful  
128 binary science case: the estimation of the ages of young moving groups.

129 To determine robust masses for imaged substellar companions, it is essential to have a well-  
130 defined age for the system. The host stars of most imaged planets to date reside in nearby young  
131 moving groups. A common method to determine the age of a young moving group is to use the  
132 HR diagram position of the stars in the group combined with models of stellar evolution to find  
133 a best-fit age for all stars in the group. Measuring dynamical masses of moving group binary  
134 stars presents an opportunity to improve on this method, as they eliminate the degeneracy between  
135 mass, metallicity, and age in the color-magnitude diagram.<sup>17</sup> By combining resolved photometry  
136 and dynamical mass measurements, one can use a consistent framework to determine the age  
137 probability distribution of each component, and as a result, directly measure the age of the entire  
138 moving group.

139 Observations of binary stars with ORKID may provide better astrometric precision over NIR  
140 measurements because of the smaller point-spread function (PSF), improving the dynamical mass  
141 estimates. Additionally, the new wavelength range will provide a critical lever arm on the stellar  
142 atmospheric models. To provide the best constraints on the stellar models, ORKID requires R,  
143 I and z band measurements. To obtain the highest spatial resolution, ORKID requires fast-read  
144 modes for Lucky/Speckle Imaging at the shortest wavelengths and a non-redundant masking mode  
145 to push to the smallest angular separations.

### 146 2.1.3 *Accreting Exoplanets*

147 Despite the thousands of known planets, scientific understanding of the early stages of planet  
148 formation is poorly constrained by observations. In particular, the details of mass delivery mech-  
149 anisms and timescales at early ages are difficult to probe due to the paucity of accretion measure-  
150 ments. So far, accretion has been directly detected in only three cases, despite several searches:<sup>18,19</sup>  
151 the controversial LkCa 15b,<sup>20-22</sup> PDS 70 b and c,<sup>23,24</sup> and Delorme 1 (AB)b.<sup>25</sup> These initial detec-  
152 tions allowed us to start constraining models,<sup>26</sup> but more measurements are needed. Leveraging  
153 Keck's near-infrared Pyramid wavefront sensor<sup>27</sup> and its 10 meter aperture, the short wavelength  
154 coverage afforded by ORKID will enable new searches for H-alpha emission from accreting proto-  
155 planets around redder stars and at smaller inner working angles than previously accessible. These  
156 searches require the ORKID filter complement to include an H-alpha narrowband filter, as well as  
157 a continuum filter. When searching for accreting planets, ORKID will operate in a lucky imaging  
158 mode, a speckle imaging mode and/or a non-redundant masking mode.

159 *2.1.4 Supermassive Black Holes and Active Galactic Nuclei (AGN)*

160 Current Keck NGS adaptive optics limits the number of accessible AGN targets due to their faint-  
161 ness and the extended nature of their core, making it hard or impossible for the AO system to  
162 provide the high-order correction needed for visible-light imaging. Keck’s current ground-based  
163 LGS system cannot provide good correction down to the visible regime. Nonetheless, we high-  
164 light here potential visible-light AGN science cases should an AO system (e.g. such was one that  
165 leverages ORCAS, or a future visible-light AO system) be able to lock on these targets.

166 The discovery that at the heart of virtually all massive galaxies in the local Universe, lie super-  
167 massive black holes (SMBHs) strongly suggests that black holes play a pivotal role in the forma-  
168 tion and evolution of galaxies. The well-known correlation between the black hole mass and the  
169 host galaxy’s stellar velocity dispersion<sup>28–31</sup> launched a long-standing view that black hole growth  
170 and the build-up of galaxy bulges go hand-in-hand, perhaps as galaxy interactions fuel the central  
171 SMBH and grow the galaxy’s bulge, and feedback from the active galactic nucleus (AGN) regulates  
172 the surrounding star formation in the host galaxy.<sup>32–36</sup> While both simulations and theory support  
173 this general paradigm, the detailed physics surrounding the formation and growth of the black hole  
174 and its impact on the host galaxy are currently not well understood. Furthermore, binary SMBHs  
175 formed in galaxy mergers are one of the key contenders for the recently announced stochastic  
176 gravitational-wave background detected by pulsar timing arrays (ref). A clear understanding of  
177 the SMBH binary contribution to the GW background and future prospects for detecting SMBH  
178 binaries by the next generation of gravitational wave detectors requires a firm understanding of  
179 SMBH binary evolution, the pairing rate and distribution as a function of redshift, all of which are  
180 not well-constrained based on current observations. In order to make progress in the field, high  
181 spatial resolution observations across a significant portion of the sky is critical. ORKID and fu-  
182 ture enabled spectroscopic instruments such as ORCAS will be a game changer in this field. High  
183 spatial resolution imaging in the optical enables the highest sensitivity and spatial resolution to  
184 probe the central parsecs in AGN hosts, within the gravitational sphere of influence of the black  
185 hole. Imaging observations alone can enable detailed morphological studies of AGN hosts down  
186 to spatial scales ( $\approx 3\text{pc}$ ) corresponding to nuclear star clusters (NSCs) in a significant sample of  
187 galaxies for the first time. Such a study can establish the link between NSC properties and black  
188 hole properties. Imaging observations can also produce a sample of advanced mergers with closely  
189 separated galaxy nuclei down to 15mas (corresponding to a few parsecs in the local universe and  
190 100 pc at cosmic noon), an unprecedented regime of parameter space, providing some preliminary  
191 constraints on the rate and distribution of closely paired nuclei in the local Universe. Follow-  
192 up spectroscopy at high spatial resolution can identify accretion signatures, measure black hole  
193 masses, luminosities, and accretion rates, identify and measure outflows near their launch origin,  
194 and characterize the state and structure of the surrounding interstellar medium at unprecedented  
195 spatial resolution for the first time, allowing a first look into the detailed physics around accreting  
196 SMBHs in galaxy centers.

197 Models for their formation make divergent predictions for the mass distribution of intermediate  
198 mass black holes, particularly in the range  $10^2 - 10^4 M_{\odot}$  at late times. ORCAS allows Keck to be  
199 uniquely suited to survey nearby dwarf galaxies and search for such black holes, which are the  
200 building blocks of both more massive galaxies and their supermassive black holes. These obser-  
201 vations will resolve the cores of these systems to angular resolutions of  $\sim 15$  mas or better. Other  
202 ground-based (e.g. VLT/MAVIS) and space-based (HST) facilities have insufficient resolution in

203 optical wavebands to accomplish this science. Optical waveband observations are necessary in  
204 order to discriminate AGN from compact star clusters. A tractable goal is to find AGNs in dwarf  
205 galaxies by searching for broad lines. As a result, this survey will seek to determine the origins of  
206 supermassive black holes and solve one of the major unsolved mysteries in contemporary astro-  
207 physics.

208 Dual AGN are expected because galaxies grow and evolve via mergers and interactions, yet  
209 observations of dual AGN are exceedingly rare. Further observations could provide evidence of  
210 black hole growth through accretion, regulation of star formation, and that they are precursors of  
211 black hole mergers, which are strong emitters of gravitational radiation. In particular, probing close  
212 in mergers could shed light on difficulties with how theoretical models account for how SMBHs go  
213 from close encounters to candidates for a merger. To date, there is only one bound binary known<sup>37</sup>  
214 and only a handful with separations less than 3 kpc.<sup>38–41</sup> Current Keck AO can only resolve dual  
215 AGN to  $\sim 50$  pc resolution. At this distance, SMBHs are not yet gravitationally bound. However,  
216 diffraction-limited optical observations can probe this close-in region. These capabilities have been  
217 demonstrated in ORCAS asteroid studies.<sup>42</sup>

218 AGN power the flow of matter and energy from central engines to pervade their host galaxies.  
219 Outflows take the form of winds and jets; by studying them, we can better understand the role of  
220 AGN in regulating star formation in their host galaxies. Of critical importance is the capacity to  
221 spatially resolve the inner parsec scales of AGN to directly trace the gas. Currently, the best spatial  
222 resolution in the optical for nearby AGNs is  $\sim 10$ s of pc (Gemini Multi-Object Spectrograph-  
223 Integral Field Unit or Keck AO). ORCAS/Keck will probe the sub-kiloparsec scale to trace gas  
224 flows with prominent optical emission lines (e.g. OIII) and spatially resolved spectroscopy.

## 225 2.2 Programmatic Goals

226 One major goal of the ORKID effort is to demonstrate and characterize the performance of the  
227 current Keck II AO system at visible wavelengths, and in doing so retiring risk, raising technol-  
228 ogy readiness level (TRL), and informing the future design of ORCAS-WMKO mission instru-  
229 ments. Another goal is to foster successful collaboration between the ORCAS mission team and  
230 the WMKO team that allows for an observation plan guided by community engagement, providing  
231 high-performance AO to all U.S. astronomers. An additional timeline goal of less than 200 days  
232 was set, requiring the team to deliver the instrument, meeting the requirements, tight schedule, and  
233 budget.

234 Furthermore, we are interested using ORKID to evaluate the current AO system's performance  
235 in the following ways:

- 236 1. Measuring the Strehl ratio and FWHM in short (10 ms) and long (several minute) exposures  
237 over a range of wavelengths (595 to 970 nm) and guide star magnitudes (0 to 10<sup>th</sup>).
- 238 2. Measuring the contrast ratio versus distance from the guide star.
- 239 3. Better understanding the limitations of the current Keck AO system and what performance  
240 improvements are needed for impactful ORCAS science.
- 241 4. Determining how much tip-tilt performance improvement is needed to maintain close to  
242 diffraction-limited angular resolution. This can be seen in the evolution of image position  
243 between consecutive short exposure images.

- 244 5. Using this experience as a step in developing a roadmap to visible science instrumentation  
245 to be developed for ORCAS.

246 Ultimately, the team was capable of designing, building, and commissioning the ORKID in-  
247 strument, in under 200 days, to meet the requirements on both sides of the partnership and deliver  
248 results within the narrow time frame. However, the timeline drove several design and development  
249 decisions for ORKID. For instance, the opto-mechanical design choices minimized the number of  
250 parts needed, reducing fabrication time. Similarly, the optical module is capable of integrating two  
251 alternative stages due to shortages in the original chosen stage, and this allows for the instrument  
252 to be better adapted in the future. Ultimately, the strict 200 day timeline was chosen to ensure  
253 a full mission proposal by 2025. To this end, the team can quantify how fast development can  
254 move throughout the entire instrument design process. Furthermore, it provides an opportunity to  
255 identify the constraints imposed by the ground-based components during instrument development.

### 256 **3 Instrument Requirements, Constraints, and Design Choices**

257 The ORKID design is driven by the scientific and programmatic requirements presented in section  
258 2, which are derived from the ORCAS mission Science traceability Matrix (STM). In this section,  
259 technical requirements and constraints are presented. We list the opto-mechanical requirements  
260 for the science camera in subsection 3.1, and discuss size and weight constraints with which the  
261 system needed to comply in subsection 3.2.

#### 262 *3.1 Science Camera Opto-Mechanical Requirements*

263 The following requirements were established for the science camera:

- 264 1. The visible science camera system shall be Nyquist sampled at 650 nm wavelength.
- 265 2. The plate scale shall be met within a tolerance of  $\pm 0.1$  mas.
- 266 3. The visible science camera system shall provide a 10" or larger unvignetted science field.
- 267 4. The transmitted wavefront quality through the visible camera system optics shall be less than  
268 50 nm rms.
- 269 5. The throughput through the ORKID instrument shall be greater than 90 percent between 595  
270 and 970 nm wavelength.
- 271 6. A 2" x 2" science field shall be capable of being read out in 10 ms.
- 272 7. Differential atmospheric refraction (DAR) correction must be provided between the science  
273 and wavefront sensing wavelengths to maintain the science target position within  $\frac{1}{4}$  of the  
274 diffraction-limited image diameter over a 5-minute observation sequence at a 45° zenith  
275 angle.
- 276 8. DAR over any 100 nm wavelength band between 600 and 1000 nm shall be less than  $\frac{1}{4}$  of  
277 the diffraction-limited image diameter at 45° zenith angle.
- 278 9. The visible science camera system shall provide a filter changer with at least six filter loca-  
279 tions.

- 280 10. The filter changer shall be located as close as possible to the pupil plane to minimize field-  
281 dependent aberrations and to allow a pupil plane mask to be located in the filter wheel.
- 282 11. The visible science camera system shall be provided with a science-determined set of filters.
- 283 12. The visible camera system shall not vignette the 120” diameter field to the AO acquisition  
284 camera.
- 285 13. The visible camera system shall be co-mounted on the same stage with the AO acquisition  
286 camera.
- 287 14. A beamsplitter shall be provided to split the 595 to 970 nm light between the visible science  
288 camera and the AO acquisition camera.

### 289 *3.2 Footprint, Volume and Weight Constraints*

290 The physical location and size for a visible science camera were limited by the constraints of the  
291 Keck II AO bench. ORKID needed to be located in reflection from the dichroic beamsplitter that  
292 transmits light to the near-infrared science instruments. It could not interfere with the light to  
293 the existing visible wavefront sensors. Therefore, the visible science camera was integrated with  
294 the existing science camera with the existing acquisition camera (ACAM) as part of the ORKID  
295 package.

296 The ORKID assembly (A) and its location on the AO bench are shown in Figure 2. The  
297 horizontal footprint of the existing ACAM system could not be exceeded to avoid interference  
298 with existing opto-mechanical systems. The vertical height was limited by the position of the  
299 optical axis above the AO bench (305 mm) and the height of the AO bench cover. The clearance  
300 of the delivered ORKID unit (vertical space between the unit and the AO bench cover) is 54 mm.  
301 ACAM is mounted on a linear stage and pedestal, which were reused to support ORKID. The stage  
302 is used to focus ACAM on either a natural guide star (at infinity) or a laser guide star (as close as  
303 85 km). If necessary, the handles shown in Figure 2(a) can be removed to reduce the footprint.

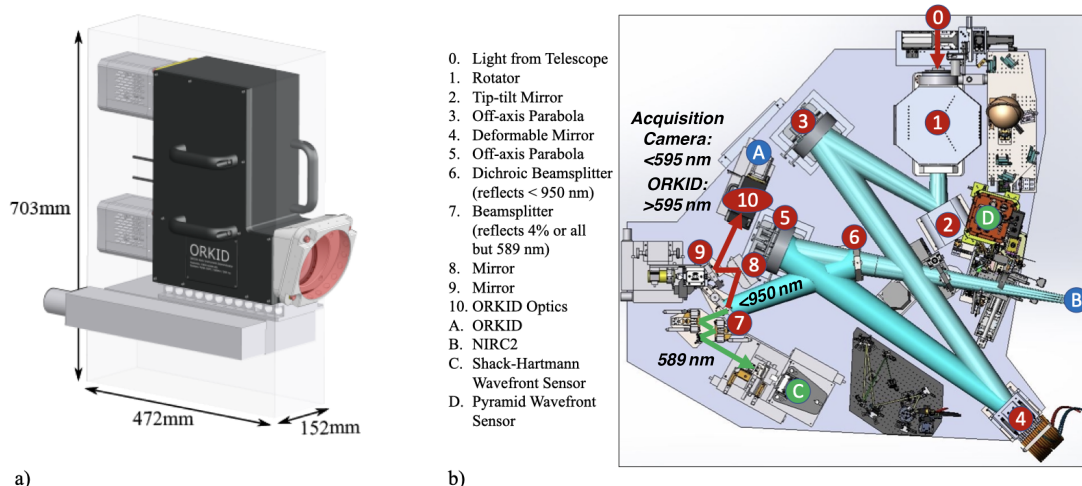


**Fig 2** ORKID system (a) and the envelope available to integrate the ORKID unit on the Keck II AO bench (b). In addition, we provide the full light path from the telescope to the ORKID instrument. The optional Astigmatism Corrector Plate (ACP) can be seen on the left as a red plate attached to the ORKID system.

304 An astigmatism corrector plate can be mounted to the front of the ORKID assembly, as further  
 305 described in section 4.1.2. However, it is not currently required, and extends outside the current  
 306 ACAM envelope.

307 The maximum weight for the ORKID unit was set by the maximum allowed weight for the  
 308 linear stage (90 kg); however, due to difficult installation access to the AO bench, the unit was  
 309 designed to minimize weight.

## 310 4 Instrument Design

### 311 4.1 Optical Design

312 The ORKID optical system, shown in Fig. 3, includes the acquisition channel (120" FOV) and  
 313 the science channel (10" FOV). The driving science performance goal was Nyquist sampling (2-  
 314 pixel) of a  $650\text{ nm}$  diffraction-limited PSF. The main design constraint was the volumetric limits  
 315 for being able to be placed on the very crowded Keck AO bench.

#### 316 4.1.1 Optical Layout

317 The ORKID instrument is placed at the focus of the AO bench visible light path at a plate scale  
 318 of  $0.727\text{ mm/arcsecond}$ . With a  $100\text{ mm}$  acceptance aperture, this allows for the capture of the  
 319 full  $120\text{ arcsecond}$  diameter circular field that was passed through the AO rotator. A  $250\text{ mm}$  focal  
 320 length field lens converges the ray bundles to form a pupil at the acquisition camera lens. The  
 321  $50\text{ mm f/1.4}$  lens re-images the full-field telescope image onto the acquisition camera sensor.

322 Within the converging ray bundle following the field lens, a dichroic beamsplitter reflects the  
 323 long wavelengths (greater than  $595\text{ nm}$ ) to the science channel. A custom triplet lens captures the  
 324 central  $10\text{ arcsecond}$  field to re-image it at the science camera at  $f/34.3$ . At a camera plate scale of  
 325  $6.7''/\text{pixel}$ , the  $650\text{ nm}$  PSF FWHM covers two pixels.

326 Before reaching focus, the beam passes through several more optical elements. A pair of six-  
 327 position filter wheels allow for bandpass filters and/or pupil masks to be placed into the beam. The

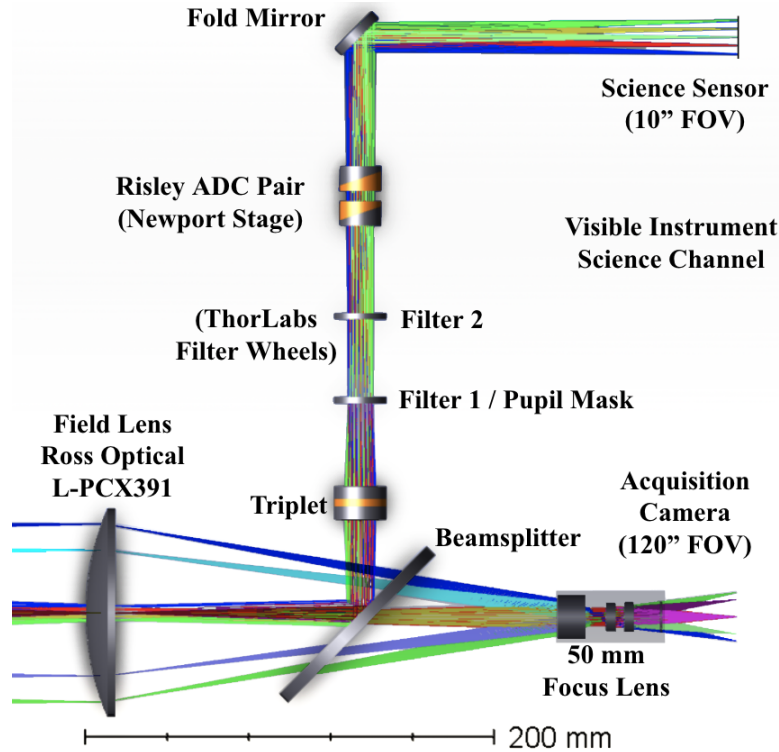


Fig 3 Optical Layout of the ORKID instrument.

328 first filter wheel is located at the pupil formed by the combination of the field lens and the triplet.  
 329 It is there that either four filters or a pupil mask can be inserted into the beam. The pupil mask is  
 330 used for non-redundant Aperture Masking Interferometry (AMI) for increased angular resolution  
 331 of a specific binary target. The second filter wheel contains five additional bandpass filters. Either  
 332 filter wheel can be used in the “open position”, and the filters in the second wheel can be used in  
 333 conjunction with the pupil mask of the first wheel. The second filter wheel is tilted by  $\sim 4^\circ$  to avoid  
 334 additional ghost reflections between the two filter wheels.

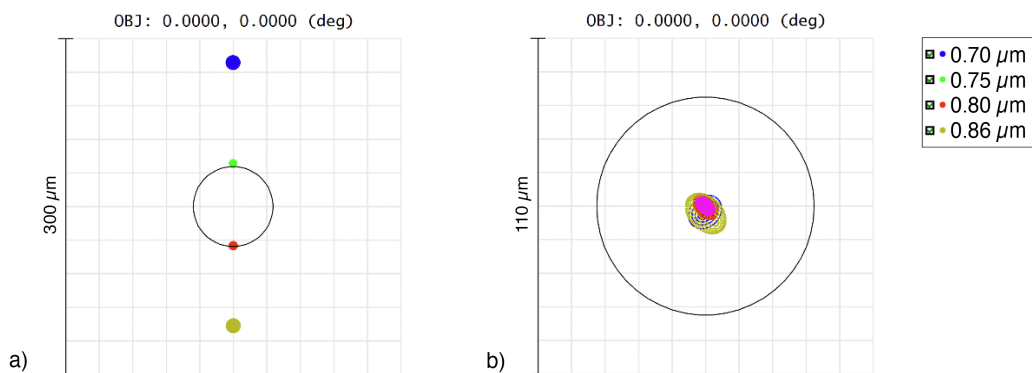


Fig 4 Spectral correction with the ADC. a) The full spectral range is shown at Zenith angle 45 deg a) uncorrected and b) when fully corrected for ORKID’s viewable i Sloan bandpass [0.698–0.853  $\mu\text{m}$ ]. The airy disc (black circle) for 700 nm is shown.

335 The next element in the optical train is the atmospheric dispersion corrector (ADC) Risley dou-  
 336 blet prism pair mounted in dual rotation stages. At ORKID’s magnification, when looking at an

337 object  $60^\circ$  off zenith, the wideband image from 595 to 970 nm is dispersed into a spectrum more  
 338 than 1.5 mm long due to the prismatic atmospheric dispersion. The ADC consists of a cemented  
 339 pair of high dispersion / low dispersion glasses with matched indexes at  $\sim 650$  nm to correct at-  
 340 mospheric dispersion. The two ADC prisms act in concert, and can simultaneously counter-rotate  
 341 to maintain the zenith dispersion direction and also rotate freely to match a desired pupil rotation.  
 342 When counter-rotated  $0^\circ$ , they cancel each other out and have no dispersive effect. When counter-  
 343 rotated a full  $\pm 90^\circ$ , the prisms combine full efficacy to correct up to  $60^\circ$  Zenith dispersion up to  
 344 the Sloan Z-band [830–1,000 nm]. Their relative rotations are therefore adjusted as a function  
 345 of waveband and Zenith. The resulting effect is shown in Fig. 4 for  $45^\circ$  Zenith when corrected  
 346 for 700–860 nm (i Sloan bandpass). Note that for narrowband filters, dispersive correction is not  
 347 needed, but they can still be used to keep an observed target centered on the sensor over various  
 348 wavebands.

349 Finally, a single flat mirror is used to fold the optical path horizontally to the science camera  
 350 sensor. The total optical path length allows the science camera and acquisition camera image  
 351 planes to be vertically co-planar. This assures that the ORKID footprint did not increase from the  
 352 original acquisition camera.

353 The total field distortion of the  $10''$  field is less than 0.2% percent, or  $\pm 0.001$  mas/pixel. This is  
 354 derived from the optical models of the telescope and camera. Within the central  $2''$ , field distortion  
 355 does not exceed 0.02%.

#### 356 4.1.2 Astigmatism Correction

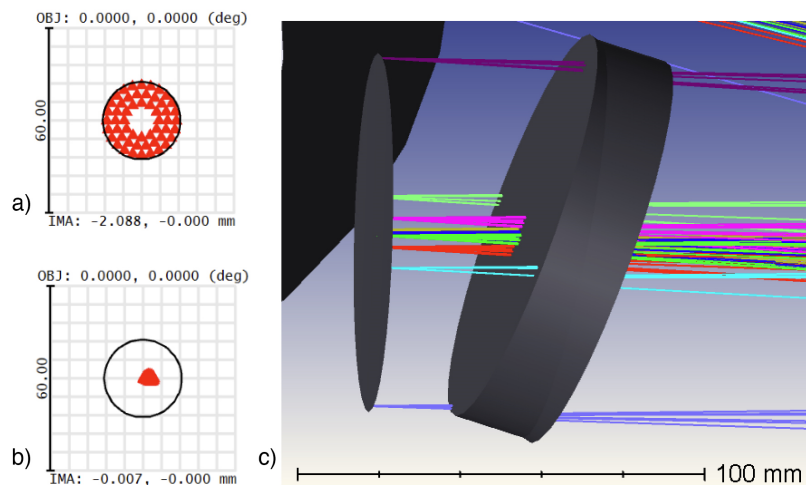


**Fig 5** Image correction by use of the Astigmatism Corrector Plate a)Uncorrected spot. b) Corrected spot. c) ACP placement at ORKID entrance aperture.

357 The AO deformable mirror (Xinetics tweeter sampled  $21 \times 21$  across the Keck pupil) can be used  
 358 to remove the astigmatism introduced by an infrared-transmissive dichroic beamsplitter in the path  
 359 to the infrared science instruments. This action introduces astigmatism in the path to ORKID. To  
 360 compensate for this, an Astigmatism Corrector Plate (ACP) can be attached to the front of ORKID  
 361 to apply the correction to the incoming beam, as shown in Figure 5. The ACP is a 20 mm thick  
 362 fused silica plano-plano element. To accommodate different correction scenarios, various ACP  
 363 plate holders can be attached or removed with a small adjustment in focus to the ORKID stage.

364 The ACP is not currently mounted since simultaneous infrared and visible science observations  
365 have not yet been performed.

### 366 4.1.3 Stray Light Mitigation

367 Stray light control keeps the image (signal) free of additional background noise that reduces the  
368 contrast and resolution of camera output. To accomplish this, baffles are integrated on element  
369 mounts (e.g., the triplet and ADCs) and other light paths to the sensors to prevent specular and  
370 “single bounce” scatter paths to the sensor. All non-bandpass refractive surfaces are anti-reflection-  
371 coated to minimize ghost reflections. Analysis shows any ghosts generated in the system have an  
372 extremely low (less than 0.1 percent) contribution to background noise.

### 373 4.2 Opto-Mechanical Design

374 The design of the opto-mechanical components of the ORKID instrument was done in a one-  
375 month schedule, which dictated many of the design choices. The instrument was thus designed  
376 to minimize the number of parts to reduce development and fabrication time. Figure 6 shows an  
377 isometric view of the CAD model and the as-built instrument.

378 The main housing was designed out of a single piece of 6061-T6 aluminum to reduce the  
379 number of interfaces and ensure a stiff structure. The cover, also machined from a single piece of  
380 aluminum, is mounted on the main housing using captive fasteners. The instrument is mounted on  
381 a linear stage (MikroPrecision P/N NE-RS-12) previously used for the visible acquisition camera.  
382 An aluminum spacer and shims provide vertical adjustability of the instrument. The ORKID unit  
383 is positioned on the spacer via dowel pins to provide a repeatable interface and can be removed  
384 independently.

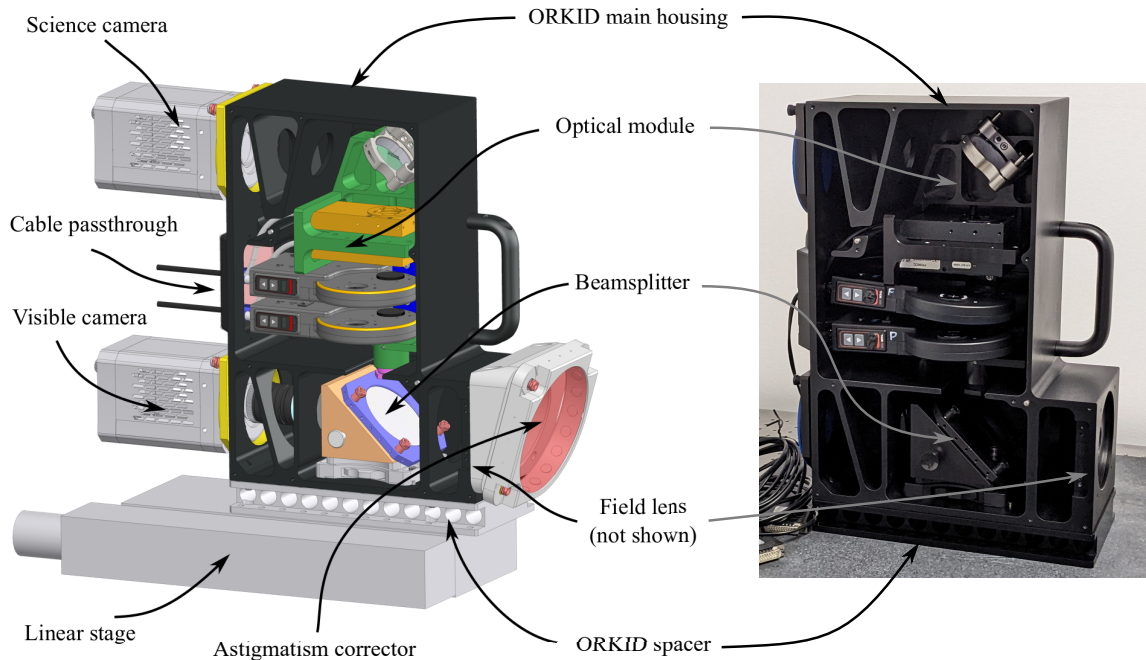


**Fig 6** Internal components of the ORKID instrument.

385 Two Andor cameras (Marana 4B-11) are mounted on an interface plate that uses three adjust-  
386 ment sleeves to account for the uncertainties of the position of the sensor of the cameras with  
387 regard to the mounting features. These sleeves allow adjustment in piston ( $\pm 5$  mm), pitch ( $\pm 2^\circ$ ),  
388 and yaw ( $\pm 2^\circ$ ).

389 The 100 mm field lens (Ross Optical P/N L-PCX391) is mounted directly at the entrance of the  
390 main housing and kept in place using an off-the-shelf threaded retaining ring (Thorlabs SM4RR).  
391 The curvature of the lens ensures self-centering when the retainer ring is installed.

392 The beamsplitter optic is mounted in a subcell using radial RTV (room temperature vulcan-  
393 izing) adhesive dots to provide a strain-free mounting. The subcell is mounted on a  $45^\circ$  support  
394 using adjustment sleeves that provides 3 degrees of freedom to the beamsplitter (i.e. piston, pitch,  
395 and yaw). The beamsplitter support is mounted on an off-the-shelf kinematic mount (Newport  
396 M-BLK-4) to provide repeatable positioning when the beamsplitter is replaced. Two mounted  
397 beamsplitters were provided to test different coatings. Figure 7 shows the beamsplitter mounted in  
398 its subcell.

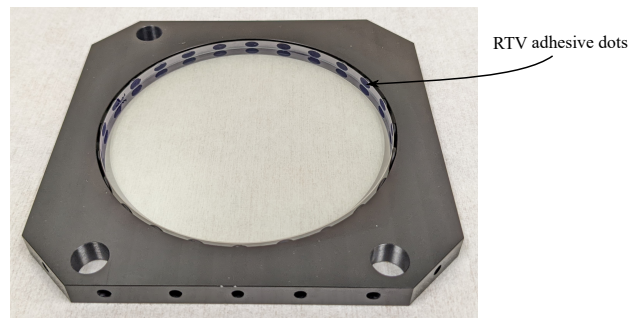


**Fig 7** Beamsplitter radially bonded in its mount using RTV adhesive dots.

399 Following the beamsplitter, the optical module (shown in Figure 8) was designed to mount the  
400 motorized components, the custom triplet, and the fold mirror. It is precisely located by dowel pins  
401 inserted in the main housing.

402 The triplet is mounted in a subcell that provides adjustability along the optical axis. The clear  
403 aperture of the subcell and its retaining ring were tailored to provide stray light reduction. The  
404 filter wheels (Thorlabs P/N FW102C) are mounted on interface plates that allow for their removal  
405 without requiring the removal of the instrument from the AO bench. The interface plates have  
406 dowel pins for repeatability, and captive fasteners ensure ease of assembly and disassembly. The  
407 first filter wheel (called the pupil wheel) is perpendicular to the optical path, whereas the second  
408 filter wheel (called the filter wheel) is placed at a 4 degree angle to reduce ghost reflections.

409 A pupil mask, shown in Figure 9, needed to be positioned precisely in the pupil wheel. Due to  
410 the lack of reference features on the off-the-shelf filter wheel, an alignment tool was designed to  
411 use the bearings and the bore of the opposite filter mount to locate the pupil mask. Two locating  
412 pins on the alignment tool interface with a hole and a slot in the pupil mask. The alignment tool  
413 was printed with a resin printer to ensure a high precision and a good fit. It should be noted that  
414 the pupil mask is placed on top of an AR-coated 3 mm thick window (shown in green in Figure 9)  
415 to maintain the optical path length. A retaining ring is torqued before removing the alignment tool.

416 Due to the shortage of the chosen baseline rotary stages because of the industrial challenges  
417 posed by the COVID-19 pandemic, the optical module was designed so that two alternative stages

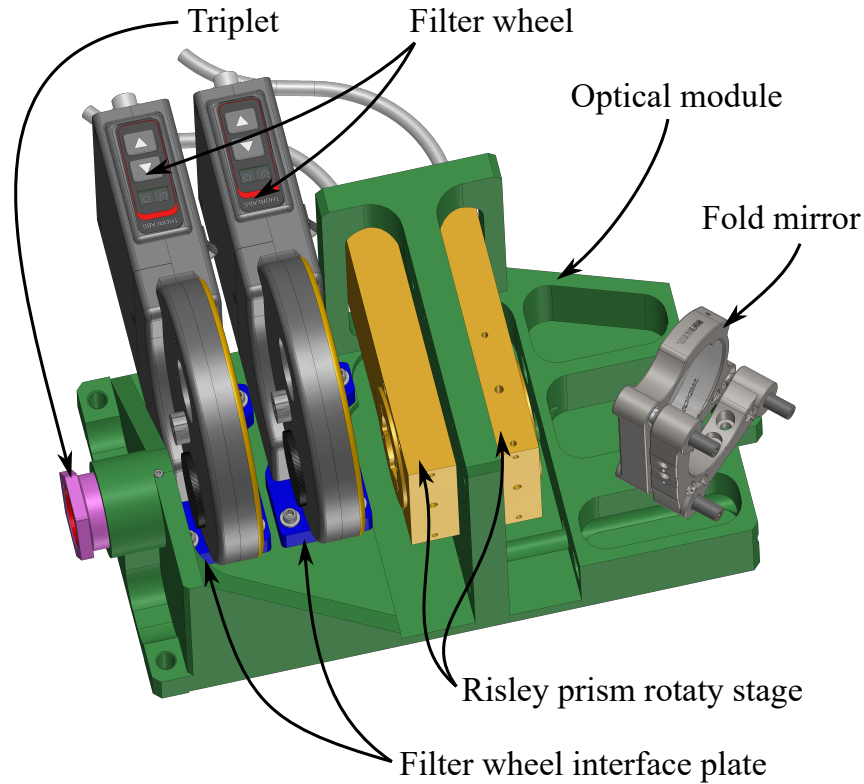


**Fig 8** Components included on the optical module.

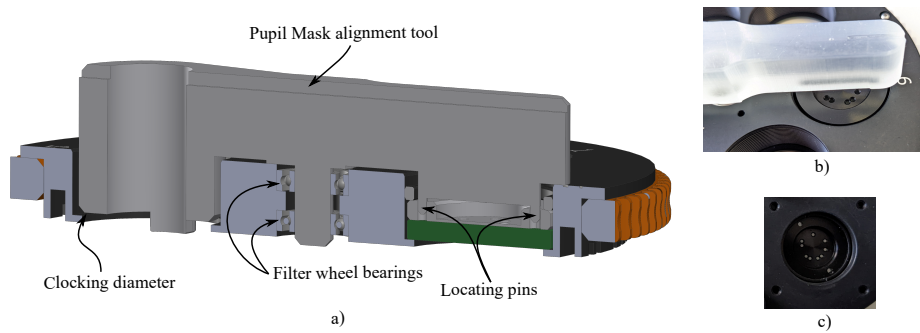


**Fig 9** Mask alignment jig. a) Cross-section of the CAD model of the alignment tool, b) Testing of the alignment tool, c) Pupil Mask installed

418 (i.e. Physik Instrumente U-651 and Newport PR50CC) could be integrated on the opto-mechanical  
 419 module. The Newport stages were implemented.

420 Each Risley Prism is mounted in a subcell that is inserted in the rotary stage. As seen in Figure  
 421 10, both subcells are identical in size and the prisms are held in place with an off-the-shelf retaining  
 422 ring (Thorlabs SM20RR). The axial placement of the subcells was not critical, so they were placed  
 423 using a caliper. A retaining ring included with the PR50CC rotary stage acts as a jam nut to the  
 424 subcell.

425 The 50 mm fold mirror (Thorlabs PF20-03-G01) is mounted in an off-the-shelf kinematic  
 426 mount (Thorlabs K2) that offers 3 degrees of freedom (i.e. piston, pitch, and yaw). To reduce

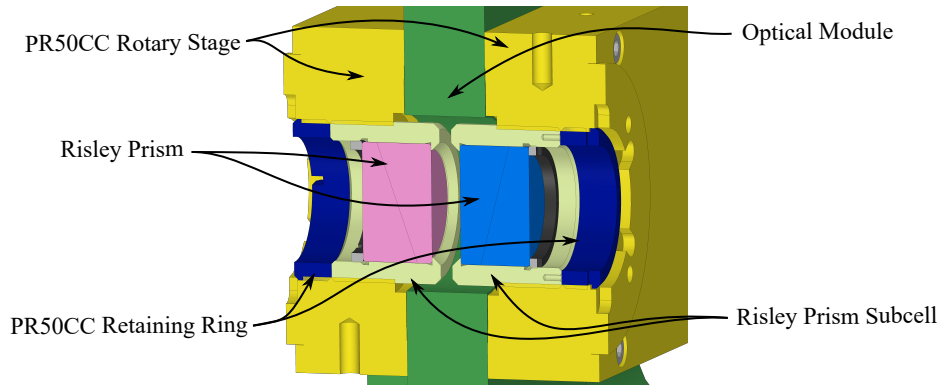


**Fig 10** Cross-section of the Risley ADC pair.

427 the stress on the mirror it was glued radially in the mount using RTV (Dow Corning 732) and the  
 428 clamping feature of the mount was not used.

429 The Astigmatism Corrector Plate was added in front of the field lens. Due to difficulties procur-  
 430 ing the optic and the short timeline, a 3D-printed support was designed to provide the ability to  
 431 modify it quickly. The printed part integrated machined adjusters and metal-threaded inserts to  
 432 provide adjustability and durability. Similar to the beamsplitter, the Astigmatism Corrector Plate  
 433 is bonded radially in its mount using RTV adhesive dots (as shown in Figure 11).

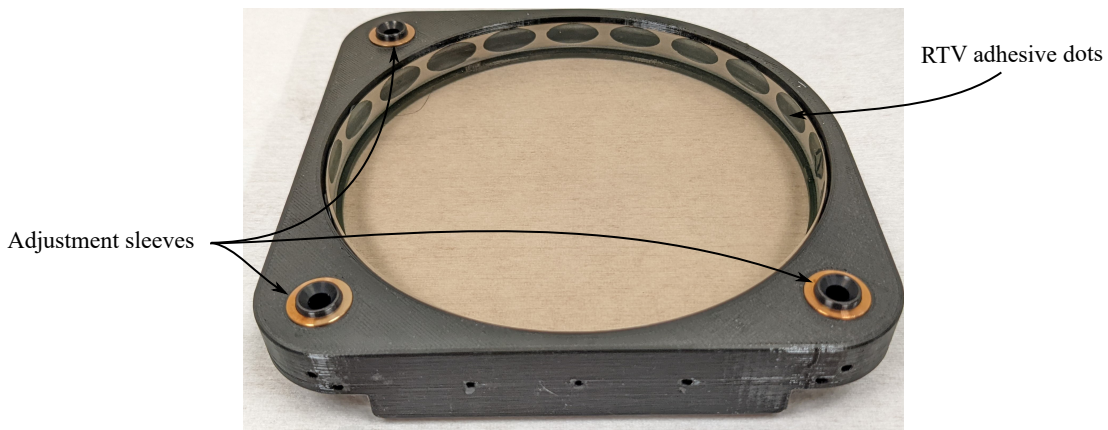


**Fig 11** Astigmatism Corrector Plate radially bonded in its 3D printed mount using RTV adhesive dots.

434 This modular approach provides a future-proof design to implement improved optical designs  
 435 with a minimum number of new opto-mechanical components.

436 Optical tolerances were provided at the beginning of the project to the mechanical team. These  
 437 requirements were pragmatic and addressed as such by minimizing the number of parts and by  
 438 the proper tolerancing of locating features inside and between modules. Not all requirements are  
 439 met right at assembly, but proper adjustment mechanisms were introduced to correct potential  
 440 dimensional errors. Adjustment mechanisms were being set at their nominal position for initial  
 441 verification. A simple alignment procedure and related hardware were developed to ensure a quick  
 442 and proper alignment if nominal positioning is not sufficient.

443 *4.3 Filters*

444 Table 1 lists the science filters installed in the ORKID filter wheels, specifically each filter wave-  
 445 length range and transmission. In addition, we plot the transmission curve for each filter in Figure  
 446 12.

**Table 1** ORKID Bandpass Filters.  $T_{Peak}$  &  $T_{Avg}$  refer to the peak and average transmission values.  $ES_{10-90}$  refer to the average bandpass edge slope from 10% to 90%.

WIDEBAND FILTERS	$\lambda_{Min}$	$\lambda_{Max}$	$\lambda_{Center}$	$T_{Peak}$	$T_{Avg}$	$ES_{10-90}$
27052 R-Band Bessell	554 nm	696 nm	625 nm	-	93%	-
27058 i Sloan	698 nm	853 nm	771 nm	-	95%	-
27059 z Sloan	830 nm	1000+ nm	-	-	90%	-
NARROWBAND FILTERS						
[OI]	620 nm	640 nm	630 nm	90%	-	-
H-alpha Continuum Filter	634 nm	646 nm	643 nm	90%	-	1.21 nm
27002 H-alpha	651 nm	661 nm	656.3 nm	94%	-	1.95 nm
27012 Jovian Methane	871 nm	907 nm	889 nm	-	94%	1.96 nm
CT940/20	920 nm	960 nm	940 nm	93%	-	2.57 nm

447 *4.4 Software Systems Design*

448 The ORKID camera server software is implemented in Python and combines the interface to the  
 449 camera with a web server and a keyword server. The web server enables browser-based GUIs,  
 450 which can be built using readily available tools. The keyword server provides the standard interface  
 451 that is common to all Keck instruments. The interface to the Andor camera is implemented through  
 452 the vendor-supplied C-based library, which communicates with the camera via USB. A Python  
 453 wrapper for this library was built using the CFFI library allowing the software to be written in  
 454 Python. The main components of the camera servers are:

- 455 • Andor camera interface: Interfaces to the vendor provided library.
- 456 • HTTP web server: Provides web services for the web-based GUI.
- 457 • Data writer: Provides asynchronous writing of FITS files to disks.
- 458 • Keck Keywords interface: Retrieves telescope and AO telemetry via keywords and provides  
 459 the ORKID keyword service.
- 460 • Control GUI: Web-based GUI to control and monitor the camera, as well as to display the  
 461 images.

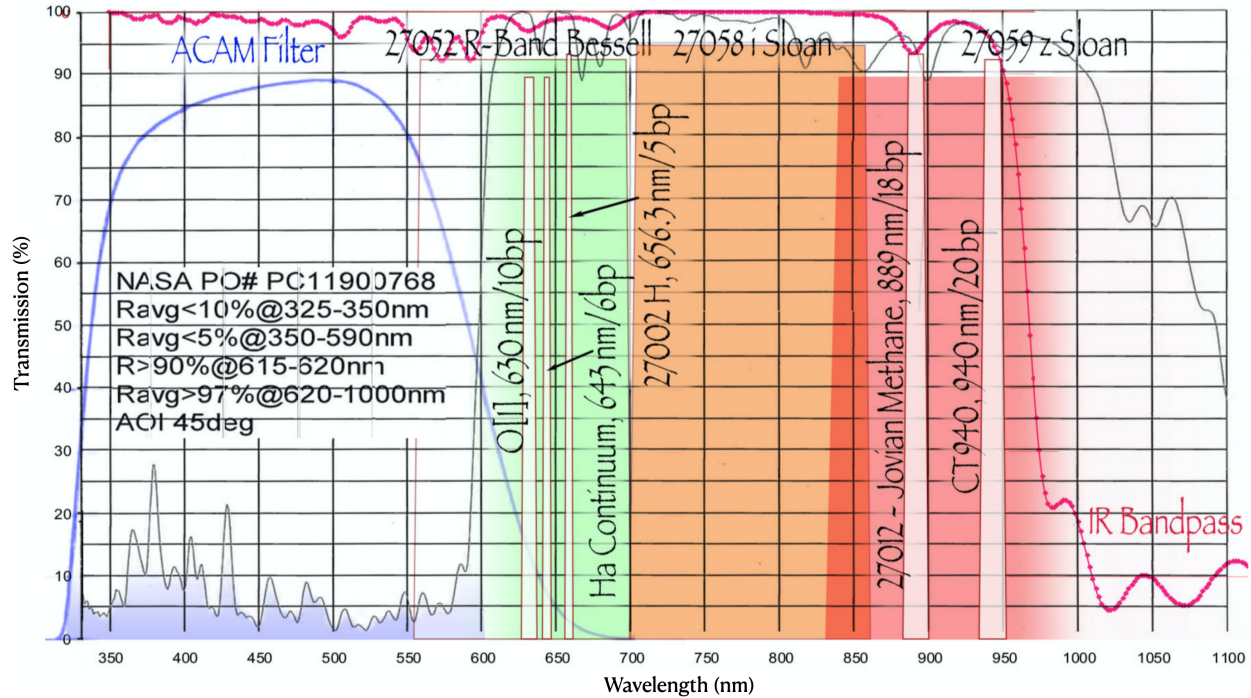


**Fig 12** The transmission curves for each filter listed in Table 1. The green, orange, and red shaded areas correspond to 27052 R-Band Bessel, 27058 i Sloan, and 27059 z Sloan broad band filters respectively. The narrowband filters reported in Table 1 are shown by the white rectangles passing in front of each shaded region, and each one is labeled.

462 The selected camera is the Andor Marana by Oxford Instruments. Table 2 shows the frame  
 463 rates for different areas of interest. The Andor Marana specification gives the maximum frame  
 464 rates. The frame rates were measured using the current implementation of the camera server for  
 465 SDR (12 bit) and HDR (16 bit) read out modes.

Area of interest (pixels)	Andor Spec max SDR rate (fps)	Measured SDR rate (fps)	Transfer SDR rate (MB/sec)	Andor Spec max HDR rate (fps)	Measured HDR rate (fps)	Transfer SDR rate (MB/sec)
32x32		738	2		594	1
64x64		594	5		427	4
128x128	750	427	15	378	274	9
256x256	378	274	36	190	159	21
512x512	190	159	84	95	87	46
1024x1024	95	87	181	30	45	95
2048x2048	48	45	211*	24	23	194

**Table 2** Maximum frame rate for different areas of interest. \*Lower rate due to dropped frames.

466 The camera frames are saved to disk in FITS format at the maximum transfer rate of 211 MB/sec.  
 467 This requires the use of fast disk storage systems. Fortunately, commercial available SSDs (Solid-  
 468 State Disks) such as the implemented Samsung PM893 7 TB, can achieve 530 MB/sec write speed.  
 469 To decouple the synchronous readout of the camera frames from the fluctuation of the data I/O pro-  
 470 cess, a FIFO data queue is used.

471 **5 Performance Analysis**

472 In review of how well ORKID performs, we compare the expected value versus the actual value  
 473 for the quantifiable science and technical requirements delineated in section 3.1 of this report, as  
 474 well as those discussed in the ORCAS Mission architecture.<sup>2</sup>

Req	Requirement Name	Expected Value	Actual Value	Satisfied	(D)esigned/(M)easured
1	Pixel Scale	$\leq 6.7$ mas/pixel	6.65 mas/pixel	Y	M
2	Plate Scale Tolerance	$\leq \pm 0.1$ mas/pixel	-0.05 mas/pixel	Y	M
3	Unvignetted Science Field	$\geq 10$ arcsec diameter	$\leq 3\%$ vignetting	Y	M
4	Transmitted Wavefront Quality	$\leq 50$ nm (rms)	$\leq 50$ nm (rms)	Y	D
5	Visible Camera Throughput	$\geq 90\%$	$\geq 90\%$	Y	D
6	2" x 2" Field Readout Time	$\leq 10$ ms	4.12 ms, 7.19 ms <sup>†</sup>	Y	M
7	DAR Correction	$\frac{1}{4} \lambda/D$	$\frac{1}{4} \lambda/D$	Y	M
8	DAR Over 100 nm Band	$\frac{1}{4} \lambda/D$	$\frac{1}{4} \lambda/D$	Y	M
9	Science Camera Filter Changer	$\geq 6$	8	Y	M
10	Pupil plane proximity	Close to pupil plane	Mask in pupil plane	Y	D
11	Filters	Science defined	8 science filters	Y	M
12	Unvignetted Acquisition Field	$\geq 120''$ diameter	120'' diameter	Y	D
13	Co-mounted Cameras	Co-mounted	Co-mounted	Y	M
14	Beamsplitter	Dichroic	Dichroic	Y	D

**Table 3** The requirements set forth in section 3.1, and if they were met. The requirement numbers in the table corresponds to the numbers in section 3.1. For more details, see Figure 13 and Figure 14.†The readout time is 4.12 milliseconds when operating in SDR mode, and 7.19 milliseconds when operating in HDR mode.

475 As can be see from Table 3, ORKID has met the requirements listed in section 3.1.

476 The plate scale as well as the plate scale tolerance were calculated by moving a white light  
 477 source, with the filter wheel in the open position, and observing the change in the pixel position.  
 478 The same source and filter wheel configuration was also used to verify that there was no vignetting  
 479 of the science field (see Figure 13).

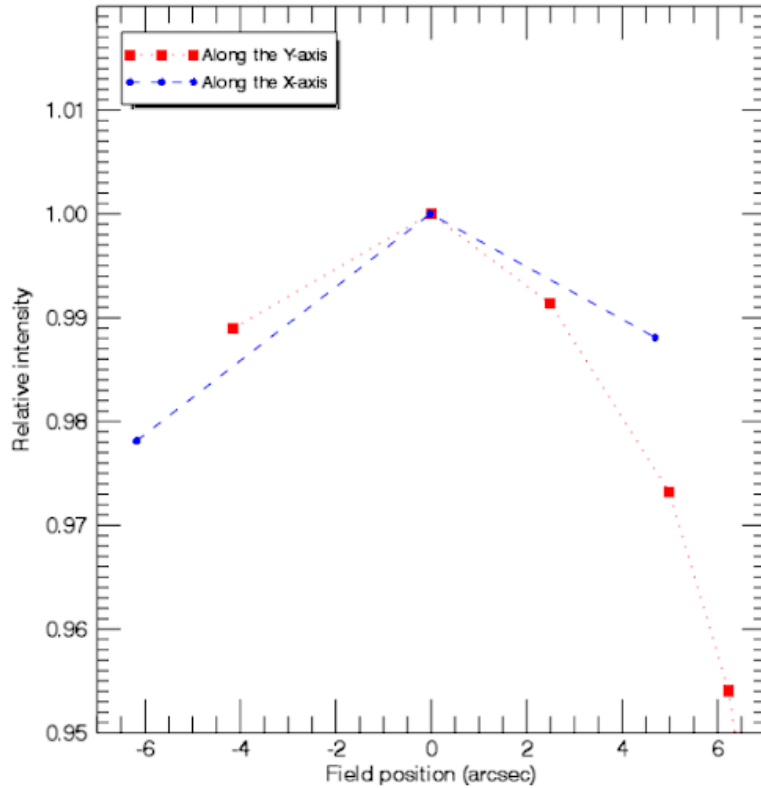


**Fig 13** Empirical test to check for vignetting. Findings demonstrate that within 5" of off-axis distance, there is less than 3% loss in intensity satisfying the 10" diameter unvignetted science field requirement.

480 Figure 14 displays the simulated wavefront error, confirming that the root mean square wave-  
 481 front error across the visible camera system optics is less than 50 nm.

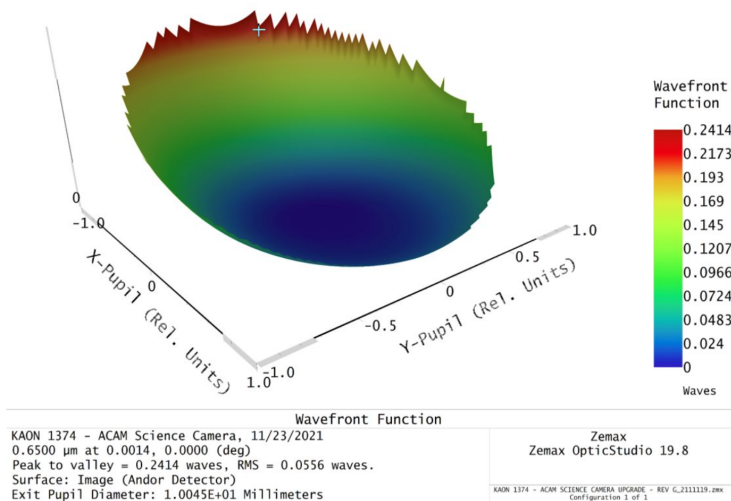


**Fig 14** Plot of wavefront error, in units of waves, across the pupil. This demonstrates that the wavefront error is <50 nm RMS across the field. The RMS wavefront error is 0.0556 waves, which, at 650 nm, equates to 36 nm RMS wavefront error.

482 It is difficult to capture the throughput of the visible science camera using a single value, as

483 the throughput is wavelength-dependent. As such, no single value was reported. Despite this, the  
484 throughput of the visible camera was over 90 percent for the wavelength range 595 – 970 nm.

485 While table 2 doesn't explicitly list the readout time for a 2" x 2" field, the readout rate was  
486 measured to be as listed in the table.

## 487 6 On-Sky Data

488 ORKID was installed behind the Keck II AO System in the fall of 2022 and has been on-sky for a  
489 total of 2.5 nights of engineering time. For the first 2 nights of observing, spread across Oct. 2022  
490 - Feb. 2023, ORKID was used in conjunction with the visible-light Shack-Hartmann wavefront  
491 sensor (SHWFS) and its atmospheric dispersion compensator (ADC) was not yet operational. The  
492 SHWFS can be fed either by a 96-4 beamsplitter, with 4% of the light being passed on to ORKID,  
493 or with the LGS dichroic, where all the visible light is passed to ORKID except for a 20 nm  
494 FWHM notch around the sodium 589 nm line used for LGS wavefront sensing. In order to pass  
495 enough light to ORKID to facilitate several ms readout times, ORKID was operated using the LGS  
496 dichroic. The reduced light going to the SHWFS resulted in a performance drop equal to making  
497 the host star roughly 2 magnitudes fainter. Here we present a small number of observations from  
498 the Oct. 22 to Feb. 2023 timeframe, that provide a preliminary view of the instrument performance,  
499 with a more detailed characterization left for future work.

500 Figure 15 shows an example of ORKID data obtained with the the Keck II AO system, using the  
501 SHWFS. The binary system SAO153301 was observed for 200 5ms exposures in the CT940/20  
502 filter on the night of January 17th, 2023 UT. The system has a combined  $V=8.71$  magnitude,<sup>43</sup>  
503 confirmed as a multiple star system with radial velocity measurements.<sup>44</sup> Figure 15 shows the  
504 binary star exposures averaged with the AO loop open (no correction), the AO loop closed (high  
505 order DM correction and tip/tilt correction), and the AO loop closed as well as a shift and add  
506 procedure applied as post-processing to the individual 5ms exposures. The procedure recentered  
507 the exposures assuming the brightest pixel to be the center of the PSF core. Comparing the three  
508 images it is clear that the AO system provided significant gains in PSF quality, yet there was a  
509 residual tip/tilt component that needed to be corrected, leveraging the fast read-out rates.

510 On November 2, 2022 UT ORKID observed  $\Theta$  Ori C, a known binary with a separation pre-  
511 viously estimated to be  $32.64 \pm 0.48$ mas using the visible-light camera of MagAO in December  
512 2012.<sup>45</sup> Note that due to orbital motion this exact position is expected to change over time.  $\Theta$  Ori C  
513 was observed for 40,000 10ms exposures in the  $H-\alpha$  filter. Individual short exposures were recen-  
514 tered using the brightest pixel as the central pixel, and then all exposures were averaged for a final  
515 image. Figure 17 displays final images created by averaging different fractions of the individual  
516 40,000 exposures, selected based on their peak pixel value. Using the final summed image (i.e. no  
517 frame selection applied; "Selection Fraction = 1" in the Figure) we fit a PSF model composed of  
518 four separate Gaussian profiles `Astropy` modeling infrastructure: two for the cores of the point  
519 sources, and two to characterize the speckle halo. We find a flux ratio between the two central  
520 Gaussian components (corresponding to the two point source cores) of  $\sim 1.5$  and a separation of  
521  $\sim 45$  mas. The central Gaussian component, representing the PSF core, has a FWHM of  $\sim 2.2$   
522 pixels, or  $\sim 15$  mas.

523 In addition to a Gaussian-shaped PSF, we also explored various combinations of Airy disks  
524 and Moffat profiles for the central core and for the extended AO speckle halo. We found that no  
525 specific combination provided a significant gain in the RMS residuals. We have also attempted

Target	Filter(s)	DM Loop State	Airmass	Total Exposure Time	Date
☉ Ori C	H- $\alpha$	Closed	1.12	40,000 $\times$ 10 ms per frame	Nov 1st, 2022
SAO 153301	CT940/20	Closed	1.25	200 $\times$ 5 ms per frame	Jan 17th, 2023
SAO 153301	CT940/20	Open	1.25	200 $\times$ 5 ms per frame	Jan 17th, 2023
Io	CT940/20	Closed	1.01	5 $\times$ 1000 ms per frame	Sep 19th, 2024
Io	H $\alpha$	Closed	1.01	5 $\times$ 500 ms per frame	Sep 19th, 2024
Io	Sloan z	Closed	1.01	5 $\times$ 100 ms per frame	Sep 19th, 2024
Betelgeuse	H-Alpha	Closed	1.03	1000 $\times$ 1 ms per frame	Nov 2nd, 2022
Betelgeuse	CT940/20	Closed	1.03	1000 $\times$ 1 ms per frame	Nov 2nd, 2022
Vesta	CT940/20	Closed	1.76	10 $\times$ 4000 ms per frame	Aug 3rd 2nd, 2023

**Table 4** Breakdown of each sky run

526 to use a high-pass filter in order to spatially filter out the broad background halo. In all cases the  
527 FWHM of the central core of the PSF was in the 14.5-16mas range.

528 The left panel of Figure 17 suggests that the core PSF is more complicated than just a simple  
529 Gaussian, as a hint of a first Airy ring can be seen. However, we did not find that an Airy ring pro-  
530 vided significantly better RMS residuals than using just a Gaussian core. Indeed, the unexpected  
531 trend that the FWHM increases as fewer frames are selected could possibly be due to the fact that  
532 the fitting process is latching onto the Airy ring-like feature, artificially increasing the FWHM.  
533 As the selection fraction gets smaller, the Airy ring-like feature becomes more prominent, thus  
534 explaining the increase in FWHM. A more detailed analysis of the PSF morphology, is beyond the  
535 scope of this publication, but is the subject of on-going research projects.

536 In Aug. 2023 the ADC was commissioned and, in addition, ORKID was operated with the  
537 near-infrared pyramid wavefront sensor. Analysis of this data is on-going and will be presented in  
538 a future publication.

539 On September 19, 2024, ORKID performed additional observations during one half of an engi-  
540 neering night. Near the end of the night, Jupiter’s volcanic moon Io was observed through a variety  
541 of filters (see Table 4). We present three images of Io captured through three filters in Figure 16.  
542 From these images, one can easily resolve the complex structure on Io’s surface. We note that min-  
543 imal reduction was performed on these images. A simple “shift-and-add” approach was employed  
544 to improve the signal-to-noise. Improvements on the data reduction will be implemented in future  
545 work.

546 We also highlight observations performed on the asteroid Vesta. The asteroid has a mean  
547 diameter of roughly 530 km, which places its angular size to be  $\sim 0.4''$ . If we refer to ORKID’s  
548 image of Vesta in Figure 19, we find that the surface is fully resolved. Furthermore, we can use  
549 ORKID’s image to estimate an angular size that is comparable ( $\sim 0.3''$ ).

550 The red giant star Betelgeuse was also targeted by ORKID. The dying star serves as a fasci-  
551 nating target for many reasons. Perhaps the most exciting prospect is the possibility to resolve its  
552 surface with ORKID. Previous studies on Betelgeuse estimate its angular diameter to have a value  
553 between  $\approx 0.04''$  and  $0.06''$ .<sup>46,47</sup> In Figure 18, we present two images of Betelgeuse captured by  
554 ORKID through the H-Alpha and CT940/20 filters. Each image was built by simply stacking all  
555 exposures after alignment through shifting. From these images, we argue that we have indeed re-  
556 solved the photosphere and measure an angular diameter of  $\sim 0.052''$ , which is in agreement with  
557 previous observations.

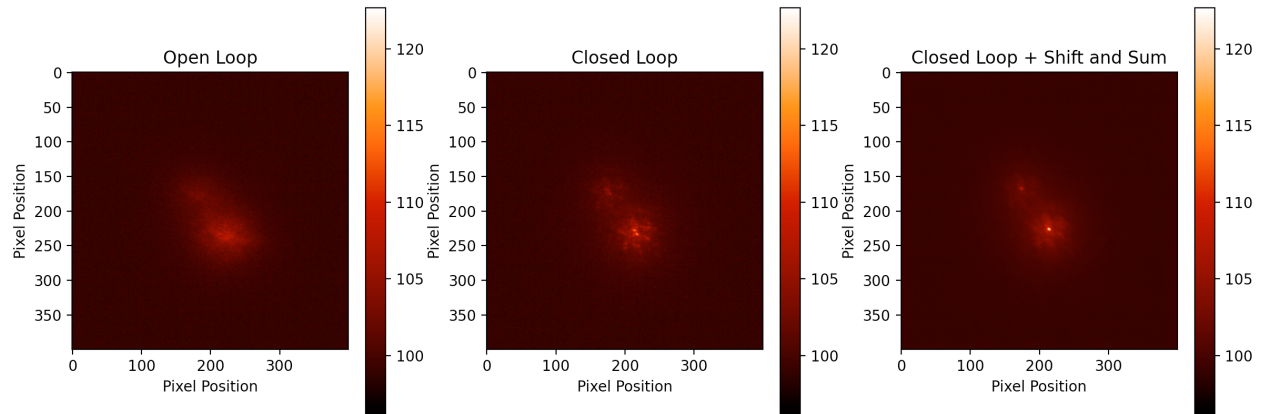


**Fig 15** ORKID images of the object SAO 153301 binary, comparing the results when the AO loop is open, versus when the AO loop is closed, versus closed loop and a recentering procedure (shifting the brightest pixel to always be aligned). To create each image 200 5 ms exposures were averaged. The colorbar displays the counts/image.

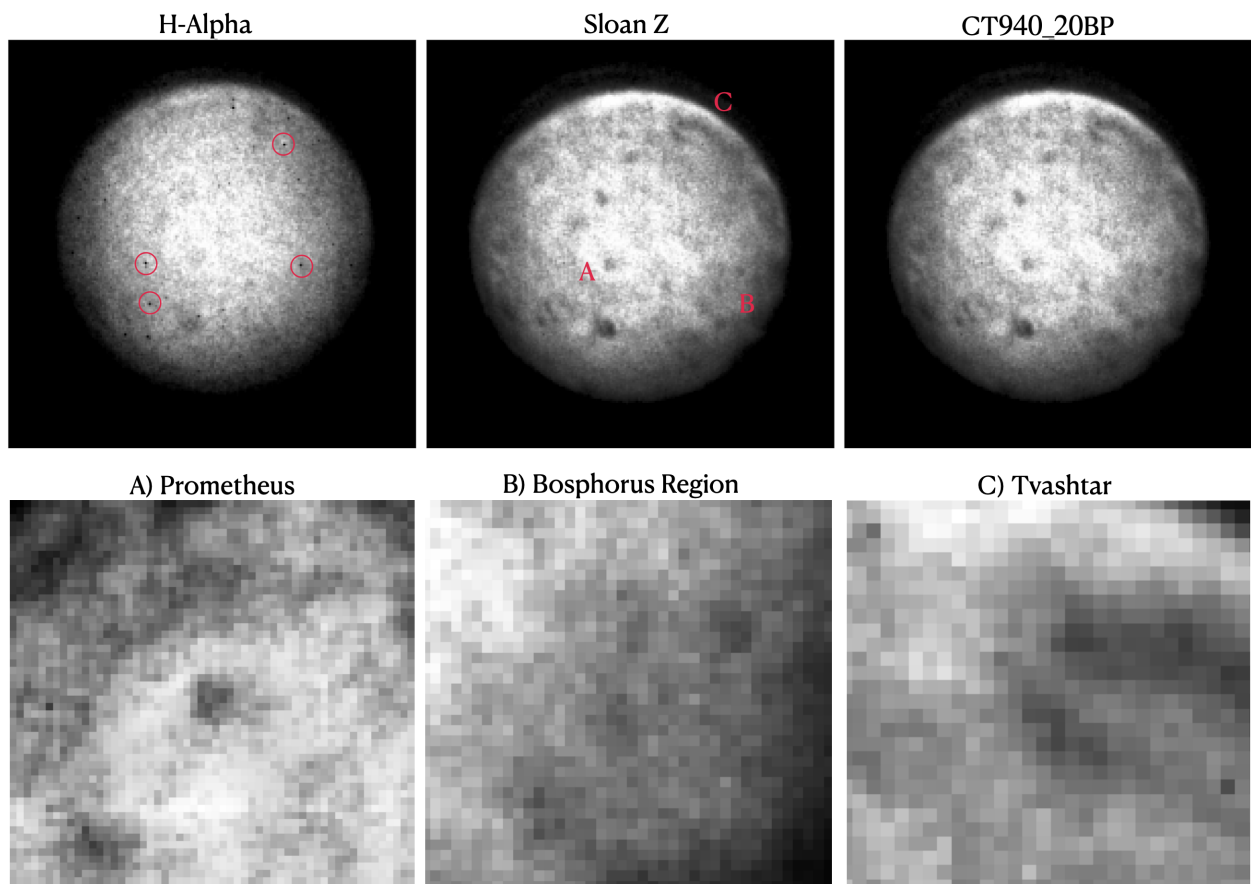


**Fig 16** Jupiter's volcanic moon Io. In the top row, we present images taken with ORKID through the H-Alpha, Sloan z, and CT940/20 filter respectively. Additionally, we zoom in on three features easily identified in the Sloan z image. Specifically, the two volcanoes Prometheus and Tvashtar, as well as the Bosphorus Region.

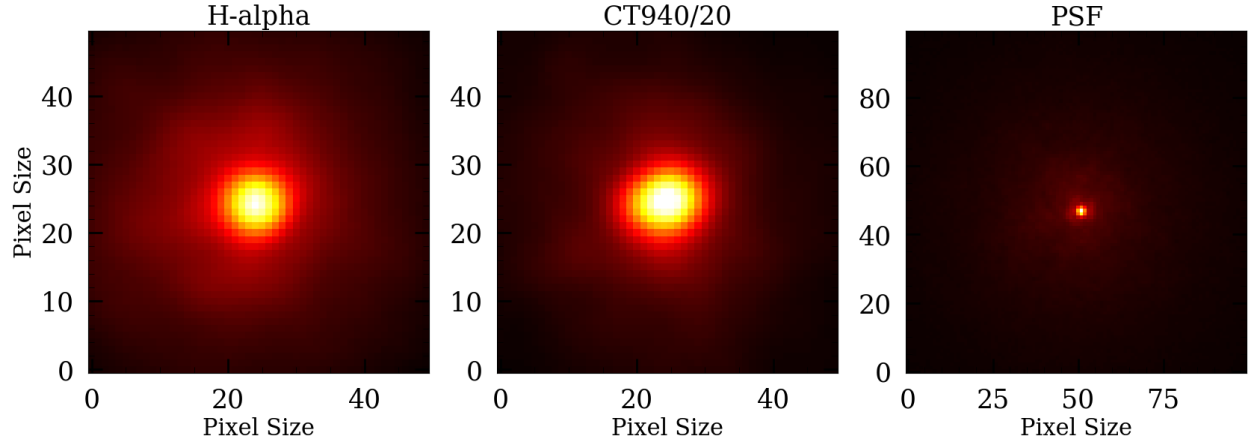


**Fig 18** Betelgeuse imaged by ORKID through two filters. From Left to Right we present the H-alpha image, CT940/20, A single-star PSF image obtained immediately after observing Betelgeuse for comparison.

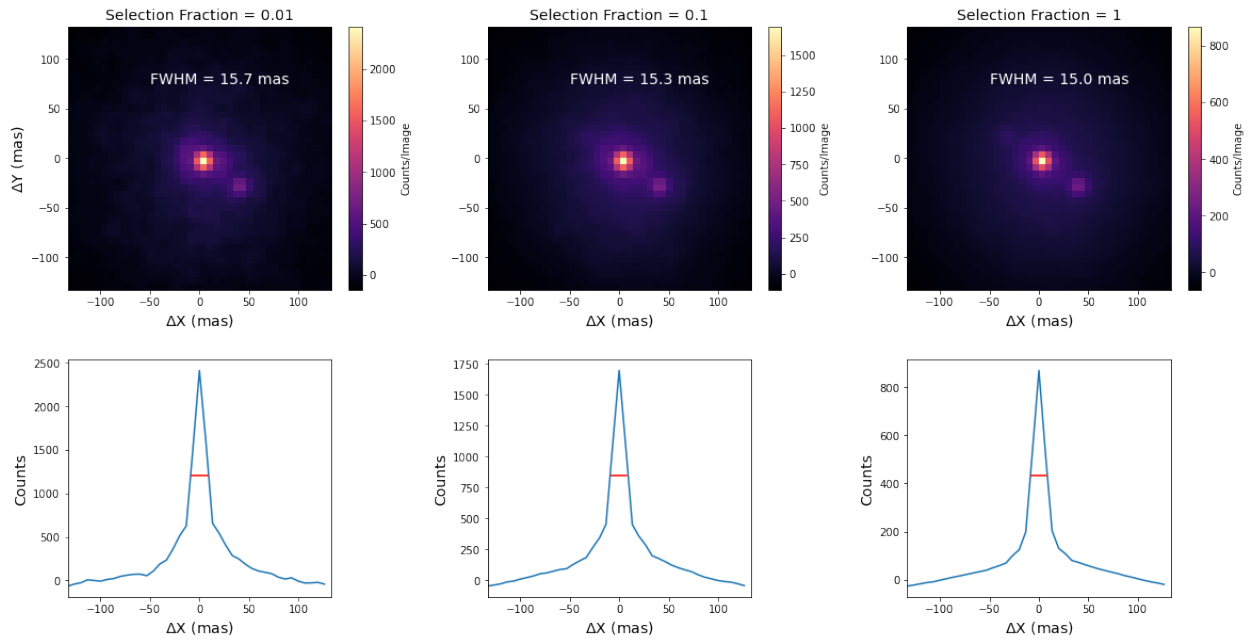


**Fig 17** Top Row: Final ORKID H- $\alpha$  images of  $\Theta$  Ori C, after averaging different fractions of the total image set, where the selections were made based on the highest peak pixel value in each exposure. The full dataset consisted of 40,000 10 millisecond exposures. Bottom Row: Brightness profiles of the row that contains the brightest pixel in the corresponding 2D image. The red horizontal lines indicate the FWHM of the PSF core, as measured using the Gaussian profile fitting.

## 558 7 Conclusion

559 The ORKID instrument has successfully demonstrated its ability to deliver high-resolution visible-  
 560 light imaging with the Keck II Adaptive Optics (AO) system, achieving a FWHM of 15.2 mas at  
 561 650 nm. This accomplishment highlights the potential of large ground-based telescopes to reach  
 562 near-diffraction-limited performance using advanced AO technology, enabling unprecedented de-  
 563 tail in visible-wavelength observations. The ability to resolve such fine details will significantly

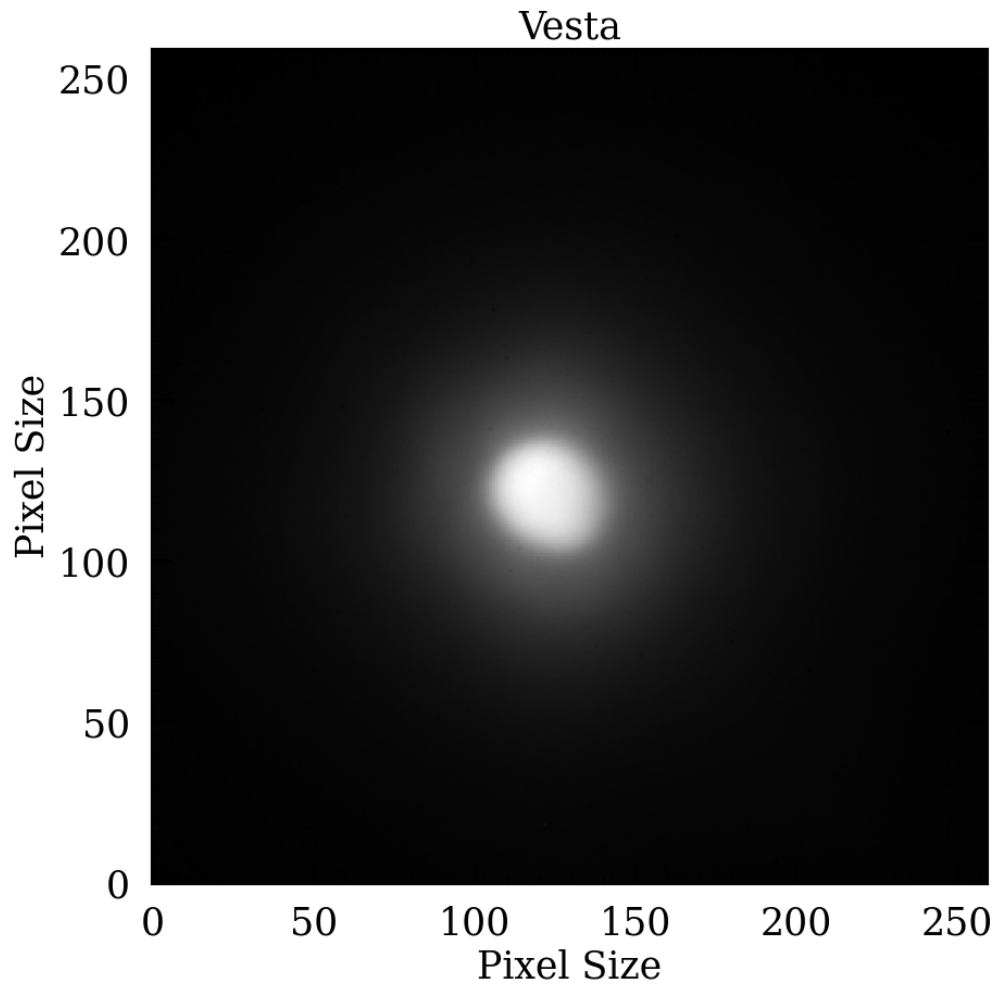


**Fig 19** The asteroid Vesta observed by ORKID through the CT940/20 filter.

564 enhance our understanding of a wide range of astronomical phenomena in the future, from the  
565 dynamics of binary stars to the atmospheres of planets and moons in the Solar System. Addressing  
566 the limitations caused by atmospheric turbulence and making visible-light AO a viable tool for  
567 future scientific endeavors.

568 In addition to its technical achievements, ORKID serves a critical role as a pathfinder for the  
569 larger ORCAS mission, which aims to create a hybrid ground-space observatory. Looking ahead,  
570 the continued evaluation and enhancement of ORKID's performance will be essential to further  
571 improving its capabilities. The upcoming upgrades to the Keck II AO system, including the inte-  
572 gration of a higher actuator count deformable mirror and faster real-time control systems, promise  
573 even better performance, especially when using bright guide stars. These advancements, coupled  
574 with the insights gained from ORKID's current achievements, will guide next steps which will  
575 include using Asteroids as guide-stars, and utilizing space born lasers as additional demonstrations  
576 and TRL advancement mechanisms. This in turn will inform the final design and development  
577 of the ORCAS mission. Ultimately, ORKID's success highlights the potential for collaborative  
578 space-ground observatory systems to revolutionize visible-light astronomy, bridging the gap be-  
579 tween current ground-based systems and future flagship space telescopes.

580 The key programmatic goals, identified in section 2.2, were accomplished. ORKID retired  
581 ORCAS risk by demonstrating and characterizing the Keck II AO system's performance at visible  
582 wavelengths, as well as informing the future design of the ORCAS-WMKO mission instruments.  
583 The joint project also successfully fostered collaboration between the ORCAS mission and WMKO  
584 teams.

585 As a pathfinder instrument the evaluation and characterization of ORKID is an on-going pro-  
586 cess. Future goals for the project include a thorough characterization of the AO performance,  
587 more detailed instrument characterization, and consideration for facilitation upon the delivery of  
588 the high-order AO system HAKA.

## 589 **8 Acknowledgments**

590 The W. M. Keck Observatory is operated as a scientific partnership among the California Institute  
591 of Technology, the University of California, and the National Aeronautics and Space Administra-  
592 tion. The Observatory was made possible by the generous financial support of the W. M. Keck  
593 Foundation. Funding for ORCAS instrument development was provided by NASA- CIF and God-  
594 dard IRAD program.

595 We would like to thank our industrial partners: Optimax team - Pierce Morgan, Steve Powers,  
596 Laura Capperell. Chroma Technology Corp. - Dick Stewart. OMP Inc. - Jean-Thomas Landry,  
597 Marc-André Boucher. Spectrum Thin Films - Tony Pirera, Derek Scomburg. Optical Planz Inc. -  
598 Kevin McKeon. All provided custom high-grade products at high speed which without this project  
599 would not of met its schedule and technical goals.

600 The authors wish to recognize and acknowledge the very significant cultural role and reverence  
601 that the summit of Mauna Kea has always had within the indigenous Hawaiian community. We are  
602 most fortunate to have the opportunity to conduct observations from this mountain.

## 603 **9 Disclosures**

604 The authors declare there are no financial interests, commercial affiliations, or other potential con-  
605 flicts of interest that have influenced the objectivity of this research or the writing of this paper

## 10 Code and Data Availability

This work made use of Astropy:<sup>1</sup> a community-developed core Python package and an ecosystem of tools and resources for astronomy.<sup>48–50</sup>

The data that support the findings of this article are not publicly available due to privacy concerns. They can be requested directly from the author at [eliad.peretz@nasa.gov](mailto:eliad.peretz@nasa.gov).

### References

- 1 Patat, F., Ugolnikov, O. S., and Postlyakov, O. V., “Orbiting configurable artificial star (orcas) for visible adaptive optics from the ground,” *Astronomy & Astrophysics* **51**, 385–393 (Aug. 2006).
- 2 Peretz, E., Hamilton, C., Mather, J., Pabarcus, L., Hall, K., Michaels, A., Pritchett, R., Yu, W., Wizinowich, P., and Golliher, E., “Orcas—orbiting configurable artificial star mission architecture,” *UV/Optical/IR Space Telescopes and Instruments: Innovative Technologies and Concepts X*. **11819** (2021).
- 3 Peretz, E., McCormick, K., Moehring, E., Hamilton, C., Mather, J., Hall, K., Hyland, D., Freeman, A., Russin, T., Nash, J., and Robie, D., “Orbiting configurable artificial star multi-wavelength laser payload,” *Astronomical Optics: Design, Manufacture, and Test of Space and Ground Systems III* **11820** (2021).
- 4 Peretz, E., Mather, J. C., Hamilton, C., Pabarcus, L., Hall, K., Fugate, R. Q., Green, W. A., and Klupar, P., “Orbiting laser configuration and sky coverage: coherent reference for Breakthrough Starshot ground-based laser array,” *Journal of Astronomical Telescopes, Instruments, and Systems* **8**(1), 017004 (2022).
- 5 Peretz, E., Hamilton, C., Mather, J. C., D’Amico, S., Michaels, A., Pritchett, R., Yu, W., and Wizinowich, P., “Astrostationary orbits for hybrid space and ground-based observatories,” *Journal of Astronomical Telescopes, Instruments, and Systems* **8**(1), 014004 (2022).
- 6 Peretz, E., Mather, J. C., Albert, J., Aldering, G., Kurczynski, P., Lafon, R., Milam, S., O’Meara, J., de Pater, I., Perlmutter, S., Plavchan, P., Satyapal, S., Windhorst, R., Wizinowich, P., Barth, A., Campbell, R., Canalizo, G., Cristina, M., Rico, G. D., Duncan, J., Freeman, A., Gebhardt, K., Gilchrist, K., Golliher, E., Hall, K., Hamilton, C., Hicks, E., Hyland, D., Juneau, S., Kassis, M., Koss, M., Kusters, D., Laha, S., Lu, J., Malkan, M., Mawet, D., Max, C., McCormick, K., Michaels, A., Michelson, D., Millar-Blanchaer, M., Moehring, E., Sanchez, F. M., Newman, P., Oppenheimer, R., Pabarcus, L., Pachowicz, P., Portaluri, E., Pritchett, R., Rice, J., Rothberg, B., Seager, S., Slonaker, R., Stephen, M., Storm, M., Vermilion, D., Villanueva, G., U, V., and Yu, W., “The orbiting configurable artificial star (orcas) mission,” tech. rep., NASA/GSFC (2021).
- 7 Wizinowich, P., Acton, D. S., Shelton, C., Stomski, P., Gathright, J., Ho, K., Lupton, W., Tsubota, K., Lai, O., Max, C., Brase, J., An, J., Avicola, K., Olivier, S., Gavel, D., Macintosh, B., Ghez, A., and Larkin, J., “First light adaptive optics images from the keck ii telescope: A new era of high angular resolution imagery,” *Publications of the Astronomical Society of the Pacific* **112**, 315 (mar 2000).

---

<sup>1</sup><http://www.astropy.org>

- 645 8 Wizinowich, P. L., Le Mignant, D., Bouchez, A. H., Campbell, R. D., Chin, J. C. Y., Contos,  
646 A. R., van Dam, M. A., Hartman, S. K., Johansson, E. M., Lafon, R. E., Lewis, H., Stomski,  
647 P. J., Summers, D. M., Brown, C. G., Danforth, P. M., Max, C. E., and Pennington, D. M.,  
648 “The W. M. Keck Observatory Laser Guide Star Adaptive Optics System: Overview,” **118**,  
649 297–309 (Feb. 2006).
- 650 9 Brase, J. M., An, J. R., Avicola, K., Beeman, B. V., Gavel, D. T., Hurd, R. L., Johnston,  
651 B., Jones, H. E., Kuklo, T. C., Max, C. E., Olivier, S. S., Waltjen, K. E., and Watson, J. A.,  
652 “Wavefront control system for the Keck telescope,” in [*Adaptive Optical System Technolo-*  
653 *gies*], Bonaccini, D. and Tyson, R. K., eds., **3353**, 517 – 521, International Society for Optics  
654 and Photonics, SPIE (1998).
- 655 10 Smith, B. A., Soderblom, L. A., Beebe, R., Bliss, D., Boyce, J. M., Brahic, A., Briggs, G. A.,  
656 Brown, R. H., Collins, S. A., Cook, A. F., Croft, S. K., Cuzzi, J. N., Danielson, G. E., Davies,  
657 M. E., Dowling, T. E., Godfrey, D., Hansen, C. J., Harris, C., Hunt, G. E., Ingersoll, A. P.,  
658 Johnson, T. V., Krauss, R. J., Masursky, H., Morrison, D., Owen, T., Plescia, J. B., Pollack,  
659 J. B., Porco, C. C., Rages, K., Sagan, C., Shoemaker, E. M., Sromovsky, L. A., Stoker, C.,  
660 Strom, R. G., Suomi, V. E., Synnott, S. P., Terrile, R. J., Thomas, P., Thompson, W. R.,  
661 and Veverka, J., “Voyager 2 in the Uranian System: Imaging Science Results,” *Science* **233**,  
662 43–64 (July 1986).
- 663 11 Smith, B. A., Soderblom, L. A., Banfield, D., Barnet, C., Basilevksy, A. T., Beebe, R. F.,  
664 Bollinger, K., Boyce, J. M., Brahic, A., Briggs, G. A., Brown, R. H., Chyba, C., Collins,  
665 S. A., Colvin, T., Cook, A. F., Crisp, D., Croft, S. K., Cruikshank, D., Cuzzi, J. N., Danielson,  
666 G. E., Davies, M. E., de Jong, E., Dones, L., Godfrey, D., Goguen, J., Grenier, I., Haemmerle,  
667 V. R., Hammel, H., Hansen, C. J., Helfenstein, C. P., Howell, C., Hunt, G. E., Ingersoll, A. P.,  
668 Johnson, T. V., Kargel, J., Kirk, R., Kuehn, D. I., Limaye, S., Masursky, H., McEwen, A.,  
669 Morrison, D., Owen, T., Owen, W., Pollack, J. B., Porco, C. C., Rages, K., Rogers, P., Rudy,  
670 D., Sagan, C., Schwartz, J., Shoemaker, E. M., Showalter, M., Sicardy, B., Simonelli, D.,  
671 Spencer, J., Sromovsky, L. A., Stoker, C., Strom, R. G., Suomi, V. E., Synott, S. P., Terrile,  
672 R. J., Thomas, P., Thompson, W. R., Verbiscer, A., and Veverka, J., “Voyager 2 at Neptune:  
673 Imaging Science Results,” *Science* **246**, 1422–1449 (Dec. 1989).
- 674 12 de Pater, I., Sromovsky, L. A., Fry, P. M., Hammel, H. B., Baranec, C., and Sayanagi, K. M.,  
675 “Record-breaking storm activity on Uranus in 2014,” **252**, 121–128 (May 2015).
- 676 13 Sromovsky, L. A., de Pater, I., Fry, P. M., Hammel, H. B., and Marcus, P., “High S/N Keck  
677 and Gemini AO imaging of Uranus during 2012-2014: New cloud patterns, increasing activ-  
678 ity, and improved wind measurements,” **258**, 192–223 (Sept. 2015).
- 679 14 Simon, A. A., Wong, M. H., and Hsu, A. I., “Formation of a New Great Dark Spot on Neptune  
680 in 2018,” **46**, 3108–3113 (Mar. 2019).
- 681 15 Molter, E., de Pater, I., Luszcz-Cook, S., Hueso, R., Tollefson, J., Alvarez, C., Sánchez-  
682 Lavega, A., Wong, M. H., Hsu, A. I., Sromovsky, L. A., Fry, P. M., Delcroix, M., Campbell,  
683 R., de Kleer, K., Gates, E., Lynam, P. D., Ammons, S. M., Coy, B. P., Duchene, G., Gonzales,  
684 E. J., Hirsch, L., Magnier, E. A., Ragland, S., Rich, R. M., and Wang, F., “Analysis of  
685 Neptune’s 2017 bright equatorial storm,” **321**, 324–345 (Mar. 2019).
- 686 16 Cantrall, C., de Kleer, K., de Pater, I., Williams, D. A., Davies, A. G., and Nelson, D.,  
687 “Variability and geologic associations of volcanic activity on Io in 2001-2016,” **312**, 267–  
688 294 (Sept. 2018).

- 689 17 Nielsen, E. L., De Rosa, R. J., Wang, J., Rameau, J., Song, I., Graham, J. R., Macintosh, B.,  
690 Ammons, M., Bailey, V. P., Barman, T. S., Bulger, J., Chilcote, J. K., Cotten, T., Doyon, R.,  
691 Duchêne, G., Fitzgerald, M. P., Follette, K. B., Greenbaum, A. Z., Hibon, P., Hung, L.-W.,  
692 Ingraham, P., Kalas, P., Konopacky, Q. M., Larkin, J. E., Maire, J., Marchis, F., Marley,  
693 M. S., Marois, C., Metchev, S., Millar-Blanchaer, M. A., Oppenheimer, R., Palmer, D. W.,  
694 Patience, J., Perrin, M. D., Poyneer, L. A., Pueyo, L., Rajan, A., Rantakyrö, F. T., Savransky,  
695 D., Schneider, A. C., Sivaramakrishnan, A., Soummer, R., Thomas, S., Wallace, J. K., Ward-  
696 Duong, K., Wiktorowicz, S. J., and Wolff, S. G., “Dynamical Mass Measurement of the  
697 Young Spectroscopic Binary V343 Normae AaAb Resolved With the Gemini Planet Imager.”  
698 **152**, 175 (Dec. 2016).
- 699 18 Cugno, G., Quanz, S. P., Hunziker, S., Stolker, T., Schmid, H. M., Avenhaus, H., Baudoz, P.,  
700 Bohn, A. J., Bonnefoy, M., Buenzli, E., Chauvin, G., Cheetham, A., Desidera, S., Dominik,  
701 C., Feautrier, P., Feldt, M., Ginski, C., Girard, J. H., Gratton, R., Hagelberg, J., Hugot,  
702 E., Janson, M., Lagrange, A. M., Langlois, M., Magnard, Y., Maire, A. L., Menard, F.,  
703 Meyer, M., Milli, J., Mordasini, C., Pinte, C., Pragt, J., Roelfsema, R., Rigal, F., Szulágyi,  
704 J., van Boekel, R., van der Plas, G., Vigan, A., Wahhaj, Z., and Zurlo, A., “A search for  
705 accreting young companions embedded in circumstellar disks. High-contrast H $\alpha$  imaging  
706 with VLT/SPHERE.” **622**, A156 (Feb. 2019).
- 707 19 Zurlo, A., Cugno, G., Montesinos, M., Perez, S., Canovas, H., Casassus, S., Christiaens, V.,  
708 Cieza, L., and Huelamo, N., “The widest H $\alpha$  survey of accreting protoplanets around nearby  
709 transition disks,” **633**, A119 (Jan. 2020).
- 710 20 Sallum, S., Follette, K. B., Eisner, J. A., Close, L. M., Hinz, P., Kratter, K., Males, J., Skemer,  
711 A., Macintosh, B., Tuthill, P., Bailey, V., Defrère, D., Morzinski, K., Rodigas, T., Spalding,  
712 E., Vaz, A., and Weinberger, A. J., “Accreting protoplanets in the LkCa 15 transition disk,”  
713 **527**, 342–344 (Nov. 2015).
- 714 21 Mendigutía, I., Oudmaijer, R. D., Schneider, P. C., Huélamo, N., Baines, D., Brittain, S. D.,  
715 and Aberasturi, M., “Spectro-astrometry of the pre-transitional star LkCa 15 does not reveal  
716 an accreting planet but extended H $\alpha$  emission,” **618**, L9 (Oct. 2018).
- 717 22 Currie, T., Marois, C., Cieza, L., Mulders, G. D., Lawson, K., Caceres, C., Rodriguez-Ruiz,  
718 D., Wisniewski, J., Guyon, O., Brandt, T. D., Kasdin, N. J., Groff, T. D., Lozi, J., Chilcote, J.,  
719 Hodapp, K., Jovanovic, N., Martinache, F., Skaf, N., Lyra, W., Tamura, M., Asensio-Torres,  
720 R., Dong, R., Grady, C., Gerard, B., Fukagawa, M., Hand, D., Hayashi, M., Henning, T.,  
721 Kudo, T., Kuzuhara, M., Kwon, J., McElwain, M. W., and Uyama, T., “No Clear, Direct  
722 Evidence for Multiple Protoplanets Orbiting LkCa 15: LkCa 15 bcd are Likely Inner Disk  
723 Signals,” **877**, L3 (May 2019).
- 724 23 Haffert, S. Y., Bohn, A. J., de Boer, J., Snellen, I. A. G., Brinchmann, J., Girard, J. H., Keller,  
725 C. U., and Bacon, R., “Two accreting protoplanets around the young star PDS 70,” *Nature*  
726 *Astronomy* **3**, 749–754 (June 2019).
- 727 24 Zhou, Y., Bowler, B. P., Wagner, K. R., Schneider, G., Apai, D., Kraus, A. L., Close, L. M.,  
728 Herczeg, G. J., and Fang, M., “Hubble Space Telescope UV and H $\alpha$  Measurements of the  
729 Accretion Excess Emission from the Young Giant Planet PDS 70 b,” **161**, 244 (May 2021).
- 730 25 Eriksson, S. C., Asensio Torres, R., Janson, M., Aoyama, Y., Marleau, G.-D., Bonnefoy, M.,  
731 and Petrus, S., “Strong H $\alpha$  emission and signs of accretion in a circumbinary planetary mass  
732 companion from MUSE,” **638**, L6 (June 2020).

- 733 26 Choksi, N. and Chiang, E., “Testing planet formation from the ultraviolet to the millimetre,”  
734 **510**, 1657–1670 (Feb. 2022).
- 735 27 Bond, C. Z., Cetre, S., Lilley, S., Wizinowich, P., Mawet, D., Chun, M., Wetherell, E., Ja-  
736 cobson, S., Lockhart, C., Warmbier, E., Ragland, S., Alvarez, C., Guyon, O., Goebel, S.,  
737 Delorme, J.-R., Jovanovic, N., Hall, D. N., Wallace, J. K., Taheri, M., Plantet, C., and Cham-  
738 bouleyron, V., “Adaptive optics with an infrared pyramid wavefront sensor at Keck,” *Journal*  
739 *of Astronomical Telescopes, Instruments, and Systems* **6**, 039003 (July 2020).
- 740 28 Magorrian, J., Tremaine, S., Richstone, D., Bender, R., Bower, G., Dressler, A., Faber, S. M.,  
741 Gebhardt, K., Green, R., Grillmair, C., Kormendy, J., and Lauer, T., “The Demography of  
742 Massive Dark Objects in Galaxy Centers,” **115**, 2285–2305 (June 1998).
- 743 29 Gebhardt, K., Bender, R., Bower, G., Dressler, A., Faber, S. M., Filippenko, A. V., Green, R.,  
744 Grillmair, C., Ho, L. C., Kormendy, J., Lauer, T. R., Magorrian, J., Pinkney, J., Richstone, D.,  
745 and Tremaine, S., “A Relationship between Nuclear Black Hole Mass and Galaxy Velocity  
746 Dispersion,” **539**, L13–L16 (Aug. 2000).
- 747 30 Gültekin, K., Richstone, D. O., Gebhardt, K., Lauer, T. R., Tremaine, S., Aller, M. C., Ben-  
748 der, R., Dressler, A., Faber, S. M., Filippenko, A. V., Green, R., Ho, L. C., Kormendy, J.,  
749 Magorrian, J., Pinkney, J., and Siopis, C., “The  $M$ - $\sigma$  and  $M$ - $L$  Relations in Galactic Bulges,  
750 and Determinations of Their Intrinsic Scatter,” **698**, 198–221 (June 2009).
- 751 31 McConnell, N. J. and Ma, C.-P., “Revisiting the scaling relations of black hole masses and  
752 host galaxy properties,” *The Astrophysical Journal* **764**, 184 (feb 2013).
- 753 32 Toomre, A., “Mergers and Some Consequences,” in [*Evolution of Galaxies and Stellar Pop-*  
754 *ulations*], Tinsley, B. M. and Larson, Richard B. Gehret, D. C., eds., 401 (Jan. 1977).
- 755 33 Barnes, J. E. and Hernquist, L., “Formation of dwarf galaxies in tidal tails,” **360**, 715–717  
756 (Dec. 1992).
- 757 34 Silk, J. and Rees, M. J., “Quasars and galaxy formation,” **331**, L1–L4 (Mar. 1998).
- 758 35 Kauffmann, G. and Haehnelt, M., “A unified model for the evolution of galaxies and quasars,”  
759 **311**, 576–588 (Jan. 2000).
- 760 36 Hopkins, P. F., Kereš, D., Murray, N., Quataert, E., and Hernquist, L., “Stellar feedback and  
761 bulge formation in clumpy discs,” **427**, 968–978 (Dec. 2012).
- 762 37 Rodriguez, C., Taylor, G. B., Zavala, R. T., Peck, A. B., Pollack, L. K., and Romani, R. W.,  
763 “A Compact Supermassive Binary Black Hole System,” **646**, 49–60 (July 2006).
- 764 38 Satyapal, S., Secrest, N. J., Ricci, C., Ellison, S. L., Rothberg, B., Blecha, L., Constantin,  
765 A., Gliozzi, M., McNulty, P., and Ferguson, J., “Buried AGNs in Advanced Mergers: Mid-  
766 infrared Color Selection as a Dual AGN Candidate Finder,” **848**, 126 (Oct. 2017).
- 767 39 Pfeifle, R. W., Satyapal, S., Secrest, N. J., Gliozzi, M., Ricci, C., Ellison, S. L., Rothberg,  
768 B., Cann, J., Blecha, L., Williams, J. K., and Constantin, A., “Buried Black Hole Growth in  
769 IR-selected Mergers: New Results from Chandra,” **875**, 117 (Apr. 2019).
- 770 40 Koss, M., Mushotzky, R., Veilleux, S., Winter, L. M., Baumgartner, W., Tueller, J., Gehrels,  
771 N., and Valencic, L., “Host Galaxy Properties of the Swift Bat Ultra Hard X-Ray Selected  
772 Active Galactic Nucleus,” **739**, 57 (Oct. 2011).
- 773 41 Koss, M. J., Blecha, L., Bernhard, P., Hung, C.-L., Lu, J. R., Trakhtenbrot, B., Treister, E.,  
774 Weigel, A., Sartori, L. F., Mushotzky, R., Schawinski, K., Ricci, C., Veilleux, S., and Sanders,  
775 D. B., “A population of luminous accreting black holes with hidden mergers,” **563**, 214–216  
776 (Nov. 2018).

- 777 42 Hall, K., Peretz, E., Wizinowich, P., Miller-Blanchaer, M. A., Mather, J., Dekany, R., Lilley,  
778 S., Marin, E., Ragland, S., Gilchrist, K., Wertheim, M., and Sheth, S., “Observing UGC 4729  
779 with a bright moving asteroid as an operation proof of concept for the ORCAS mission,” *The*  
780 *Astrophysical Journal* .
- 781 43 Zacharias, N., Finch, C. T., Girard, T. M., Henden, A., Bartlett, J. L., Monet, D. G., and  
782 Zacharias, M. I., “VizieR Online Data Catalog: UCAC4 Catalogue (Zacharias+, 2012),”  
783 *VizieR Online Data Catalog* , I/322A (July 2012).
- 784 44 Gontcharov, G. A., “Pulkovo Compilation of Radial Velocities for 35 495 Hipparcos stars in  
785 a common system,” *Astronomy Letters* **32**, 759–771 (Nov. 2006).
- 786 45 Close, L. M., Males, J. R., Morzinski, K., Kopon, D., Follette, K., Rodigas, T. J., Hinz, P.,  
787 Wu, Y. L., Puglisi, A., Esposito, S., Riccardi, A., Pinna, E., Xompero, M., Briguglio, R.,  
788 Uomoto, A., and Hare, T., “Diffraction-limited Visible Light Images of Orion Trapezium  
789 Cluster with the Magellan Adaptive Secondary Adaptive Optics System (MagAO),” **774**, 94  
790 (Sept. 2013).
- 791 46 Balega, I., Blazit, A., Bonneau, D., Koechlin, L., Labeyrie, A., and Foy, R., “The angular  
792 diameter of Betelgeuse.,” **115**, 253–256 (Nov. 1982).
- 793 47 Weiner, J., Danchi, W. C., Hale, D. D. S., McMahon, J., Townes, C. H., Monnier, J. D., and  
794 Tuthill, P. G., “Precision measurements of the diameters of orionis and ceti at 11 microns,”  
795 *The Astrophysical Journal* **544**, 1097 (dec 2000).
- 796 48 Astropy Collaboration, Robitaille, T. P., Tollerud, E. J., Greenfield, P., Droettboom, M., Bray,  
797 E., Aldcroft, T., Davis, M., Ginsburg, A., Price-Whelan, A. M., Kerzendorf, W. E., Conley,  
798 A., Crighton, N., Barbary, K., Muna, D., Ferguson, H., Grollier, F., Parikh, M. M., Nair,  
799 P. H., Unther, H. M., Deil, C., Woillez, J., Conseil, S., Kramer, R., Turner, J. E. H., Singer,  
800 L., Fox, R., Weaver, B. A., Zabalza, V., Edwards, Z. I., Azalee Bostroem, K., Burke, D. J.,  
801 Casey, A. R., Crawford, S. M., Dencheva, N., Ely, J., Jenness, T., Labrie, K., Lim, P. L.,  
802 Pierfederici, F., Pontzen, A., Ptak, A., Refsdal, B., Servillat, M., and Streicher, O., “Astropy:  
803 A community Python package for astronomy,” **558**, A33 (Oct. 2013).
- 804 49 Astropy Collaboration, Price-Whelan, A. M., Sipócz, B. M., Günther, H. M., Lim, P. L.,  
805 Crawford, S. M., Conseil, S., Shupe, D. L., Craig, M. W., Dencheva, N., Ginsburg, A.,  
806 VanderPlas, J. T., Bradley, L. D., Pérez-Suárez, D., de Val-Borro, M., Aldcroft, T. L., Cruz,  
807 K. L., Robitaille, T. P., Tollerud, E. J., Ardelean, C., Babej, T., Bach, Y. P., Bachetti, M.,  
808 Bakanov, A. V., Bamford, S. P., Barentsen, G., Barmby, P., Baumbach, A., Berry, K. L.,  
809 Biscani, F., Boquien, M., Bostroem, K. A., Bouma, L. G., Brammer, G. B., Bray, E. M.,  
810 Breytenbach, H., Buddelmeijer, H., Burke, D. J., Calderone, G., Cano Rodríguez, J. L., Cara,  
811 M., Cardoso, J. V. M., Cheedella, S., Copin, Y., Corrales, L., Crichton, D., D’Avella, D., Deil,  
812 C., Depagne, É., Dietrich, J. P., Donath, A., Droettboom, M., Earl, N., Erben, T., Fabbro, S.,  
813 Ferreira, L. A., Finethy, T., Fox, R. T., Garrison, L. H., Gibbons, S. L. J., Goldstein, D. A.,  
814 Gommers, R., Greco, J. P., Greenfield, P., Groener, A. M., Grollier, F., Hagen, A., Hirst,  
815 P., Homeier, D., Horton, A. J., Hosseinzadeh, G., Hu, L., Hunkeler, J. S., Ivezić, Ž., Jain,  
816 A., Jenness, T., Kanarek, G., Kendrew, S., Kern, N. S., Kerzendorf, W. E., Khvalko, A.,  
817 King, J., Kirkby, D., Kulkarni, A. M., Kumar, A., Lee, A., Lenz, D., Littlefair, S. P., Ma, Z.,  
818 Macleod, D. M., Mastrogiuseppe, M., McCully, C., Montagnac, S., Morris, B. M., Mueller, M.,  
819 Mumford, S. J., Muna, D., Murphy, N. A., Nelson, S., Nguyen, G. H., Ninan, J. P., Nöthe,  
820 M., Ogaz, S., Oh, S., Parejko, J. K., Parley, N., Pascual, S., Patil, R., Patil, A. A., Plunkett,

821 A. L., Prochaska, J. X., Rastogi, T., Reddy Janga, V., Sabater, J., Sakurikar, P., Seifert, M.,  
822 Sherbert, L. E., Sherwood-Taylor, H., Shih, A. Y., Sick, J., Silbiger, M. T., Singanamalla,  
823 S., Singer, L. P., Sladen, P. H., Sooley, K. A., Sornarajah, S., Streicher, O., Teuben, P.,  
824 Thomas, S. W., Tremblay, G. R., Turner, J. E. H., Terrón, V., van Kerkwijk, M. H., de la  
825 Vega, A., Watkins, L. L., Weaver, B. A., Whitmore, J. B., Woillez, J., Zabalza, V., and  
826 Astropy Contributors, “The Astropy Project: Building an Open-science Project and Status of  
827 the v2.0 Core Package,” **156**, 123 (Sept. 2018).

828 50 Astropy Collaboration, Price-Whelan, A. M., Lim, P. L., Earl, N., Starkman, N., Bradley, L.,  
829 Shupe, D. L., Patil, A. A., Corrales, L., Basseur, C. E., N’othe, M., Donath, A., Tollerud,  
830 E., Morris, B. M., Ginsburg, A., Vaher, E., Weaver, B. A., Tocknell, J., Jamieson, W., van  
831 Kerkwijk, M. H., Robitaille, T. P., Merry, B., Bachetti, M., G’unther, H. M., Aldcroft, T. L.,  
832 Alvarado-Montes, J. A., Archibald, A. M., B’odi, A., Bapat, S., Barentsen, G., Baz’an, J.,  
833 Biswas, M., Boquien, M., Burke, D. J., Cara, D., Cara, M., Conroy, K. E., Conseil, S., Craig,  
834 M. W., Cross, R. M., Cruz, K. L., D’Eugenio, F., Dencheva, N., Devillepoix, H. A. R., Di-  
835 etrich, J. P., Eigenbrot, A. D., Erben, T., Ferreira, L., Foreman-Mackey, D., Fox, R., Freij,  
836 N., Garg, S., Geda, R., Glattly, L., Gondhalekar, Y., Gordon, K. D., Grant, D., Greenfield, P.,  
837 Groener, A. M., Guest, S., Gurovich, S., Handberg, R., Hart, A., Hatfield-Dodds, Z., Home-  
838 ier, D., Hosseinzadeh, G., Jenness, T., Jones, C. K., Joseph, P., Kalmbach, J. B., Karamehme-  
839 toglu, E., Kaluszy’nski, M., Kelley, M. S. P., Kern, N., Kerzendorf, W. E., Koch, E. W.,  
840 Kulumani, S., Lee, A., Ly, C., Ma, Z., MacBride, C., Maljaars, J. M., Muna, D., Murphy,  
841 N. A., Norman, H., O’Steen, R., Oman, K. A., Pacifici, C., Pascual, S., Pascual-Granado,  
842 J., Patil, R. R., Perren, G. I., Pickering, T. E., Rastogi, T., Roulston, B. R., Ryan, D. F.,  
843 Rykoff, E. S., Sabater, J., Sakurikar, P., Salgado, J., Sanghi, A., Saunders, N., Savchenko,  
844 V., Schwaradt, L., Seifert-Eckert, M., Shih, A. Y., Jain, A. S., Shukla, G., Sick, J., Simpson,  
845 C., Singanamalla, S., Singer, L. P., Singhal, J., Sinha, M., SipHocz, B. M., Spitler, L. R.,  
846 Stansby, D., Streicher, O., Sumak, J., Swinbank, J. D., Taranu, D. S., Tewary, N., Tremblay,  
847 G. R., Val-Borro, M. d., Van Kooten, S. J., Vasovi’c, Z., Verma, S., de Miranda Cardoso,  
848 J. V., Williams, P. K. G., Wilson, T. J., Winkel, B., Wood-Vasey, W. M., Xue, R., Yoachim,  
849 P., Zhang, C., Zonca, A., and Astropy Project Contributors, “The Astropy Project: Sustain-  
850 ing and Growing a Community-oriented Open-source Project and the Latest Major Release  
851 (v5.0) of the Core Package,” **935**, 167 (Aug. 2022).